Cell Reports

Article

PUS10-induced tRNA fragmentation impacts retrotransposon-driven inflammation

Graphical abstract

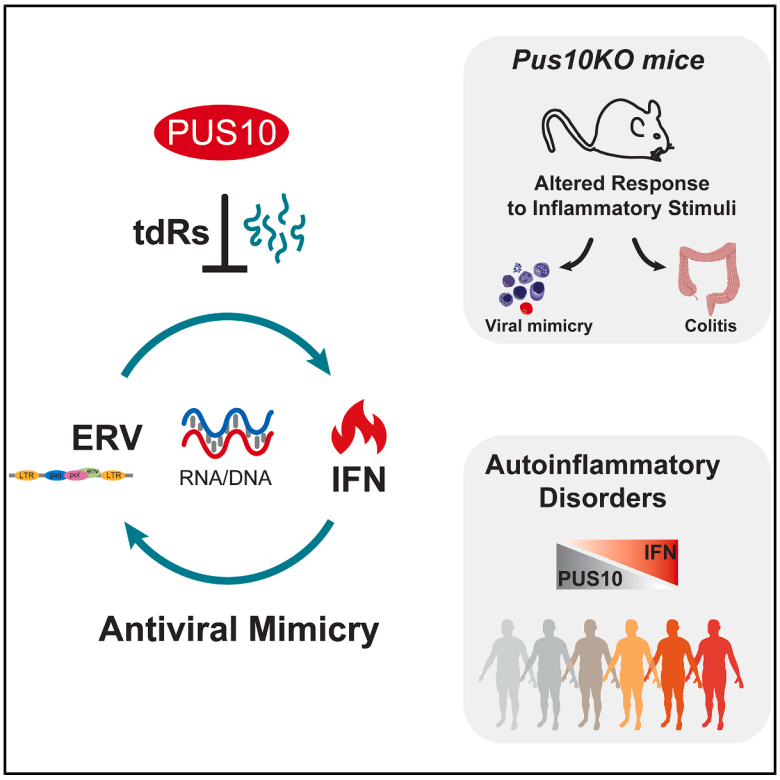

Authors

Magdalena Madej, Phuong Cao Thi Ngoc, Sowndarya Muthukumar, ..., Paolo Salomoni, David Bryder, Cristian Bellodi

Correspondence

cristian.bellodi@med.lu.se

In brief

Madej et al. reveal that PUS10, a pseudouridine synthase, regulates innate immunity impacting the inflammatory response *in vivo*. PUS10 loss disrupts tRNA-derived small RNAs, affecting translation and retroelement expression. This drives RNA-DNA hybrids accumulation, possibly activating cGAS-STING-induced inflammation and linking PUS10 dysregulation to human autoimmune disorders.

Highlights

- PUS10 depletion boosts the antiviral response without affecting development
- PUS10 deploys tRNA-derived small RNAs to suppress transposon de-repression
- PUS10 loss triggers cGAS-STING-driven inflammation, potentially via RNA-DNA hybrids
- PUS10 modulates immune responses *in vivo* and is linked to autoinflammatory disease

Madej et al., 2025, Cell Reports *44*, 115735
June 24, 2025
https://doi.org/10.1016/j.celrep.2025.115735

CellPress

Cell Reports

CellPress
OPEN ACCESS

Article

PUS10-induced tRNA fragmentation impacts retrotransposon-driven inflammation

Magdalena Madej,[1] Phuong Cao Thi Ngoc,[1,17] Sowndarya Muthukumar,[1,17] Anna Konturek-Cieśla,[1,2] Silvia Tucciarone,[1] Alexandre Germanos,[1] Christian Ashworth,[3] Knut Kotarsky,[4] Sudip Ghosh,[4] Zhimeng Fan,[5] Helena Fritz,[1] Izei Pascual-Gonzalez,[6] Alain Huerta,[6,7,8] Nicola Guzzi,[1] Anita Colazzo,[1] Giulia Beneventi,[1] Hang-Mao Lee,[9] Maciej Cieśla,[1,10] Christopher Douse,[11] Hiroki Kato,[12] Vinay Swaminathan,[5,13] William W. Agace,[3,4] Ainara Castellanos-Rubio,[6,7,14,15] Paolo Salomoni,[9] David Bryder,[1] and Cristian Bellodi[1,16,18,*]

[1]Division of Molecular Hematology, Department of Laboratory Medicine, Lund Stem Cell Center, Faculty of Medicine, Lund University, Lund, Sweden
[2]Department of Biosystems Science and Engineering, ETH Zurich, Basel, Switzerland
[3]LEO Foundation Skin Immunology Research Center, Department of Immunology and Microbiology, University of Copenhagen, Copenhagen, Denmark
[4]Department of Experimental Medical Science, Lund University, Lund, Sweden
[5]Division of Oncology, Department of Clinical Sciences, Lund University, Lund, Sweden
[6]University of the Basque Country, UPV-EHU, Leioa, Spain
[7]Biobizkaia Research Institute, Cruces-Barakaldo, Spain
[8]Galdakao University Hospital, Galdakao, Spain
[9]German Center for Neurodegenerative Diseases (DZNE), Bonn, Germany
[10]International Institute of Molecular Mechanisms and Machines, Polish Academy of Sciences, Warsaw, Poland
[11]Epigenetics and Chromatin Dynamics, Department of Experimental Medical Science, Wallenberg Neuroscience Center and Lund Stem Cell Center, Lund University, Lund, Sweden
[12]Institute of Cardiovascular Immunology, Medical Faculty, University Hospital Bonn, University of Bonn, Bonn, Germany
[13]Wallenberg Center for Molecular Medicine, Lund University, Lund, Sweden
[14]Centro de Investigación Biomédica en Red de Diabetes y Enfermedades Metabólicas Asociadas CIBERDEM, Instituto de Salud Carlos III, Madrid, Spain
[15]Ikerbasque, Basque Foundation for Science, Bilbao, Spain
[16]Biotech Research Innovation Centre (BRIC), University of Copenhagen, Copenhagen, Denmark
[17]These authors contributed equally
[18]Lead contact
*Correspondence: cristian.bellodi@med.lu.se
https://doi.org/10.1016/j.celrep.2025.115735

SUMMARY

Pseudouridine synthases (PUSs) catalyze the isomerization of uridine (U)-to-pseudouridine (Ψ) and have emerging roles in development and disease. How PUSs adapt gene expression under stress remains mostly unexplored. We identify an unconventional role for the Ψ "writer" PUS10 impacting intracellular innate immunity. Using *Pus10* knockout mice, we uncover cell-intrinsic upregulation of interferon (IFN) signaling, conferring resistance to inflammation *in vivo*. Pus10 loss alters tRNA-derived small RNAs (tdRs) abundance, perturbing translation and endogenous retroelements expression. These alterations promote proinflammatory RNA-DNA hybrids accumulation, potentially activating cyclic GMP-AMP synthase (cGAS)-stimulator of interferon gene (STING). Supplementation with selected tdR pools partly rescues these effects through interactions with RNA processing factors that modulate immune responses, revealing a regulatory circuit that counteracts cell-intrinsic inflammation. By extension, we define a PUS10-specific molecular fingerprint linking its dysregulation to human autoimmune disorders, including inflammatory bowel diseases. Collectively, these findings establish PUS10 as a viral mimicry modulator, with broad implications for innate immune homeostasis and autoimmunity.

INTRODUCTION

There is a growing realization that RNA-modifying proteins (RMPs) rewire cellular transcriptomes, steering genetic information to impact central processes in development and disease.[1,2] Remarkable examples are pseudouridine synthases (PUSs), an evolutionarily conserved class of RMPs catalyzing the isomerization of uridine (U)-to-pseudouridine (Ψ), the most widespread single nucleoside RNA modification in living organisms.[3,4] Thirteen non-redundant PUS enzymes have been identified in humans.[4] PUSs modify their RNA targets as "standalone" enzymes recognizing specific Ψ-consensus motifs or through an

RNA-dependent mechanism guided by complementary antisense box H/ACA small nucleolar RNAs (snoRNAs).[4] A wealth of studies in different organisms highlighted the importance of Ψ for the biogenesis, structure, and function of noncoding regulatory and coding RNAs with direct implications for cell homeostasis.[5] Accordingly, genetic alterations of PUSs have been linked to the etiology of inherited human syndromes, neurological disorders, and cancer.[6–8] However, the molecular basis by which dysregulation of specific PUS family proteins contributes to disease-associated pathological features remains incompletely understood.

Prior work from our laboratory uncovered an essential requirement for PUS7-mediated Ψ in governing embryonic and hematopoietic development through the regulation of protein biosynthesis.[9] In this context, PUS7-dependent pseudouridylation of unique tRNA-derived small RNAs (tdRs) functioned as a molecular "rheostat" to fine-tune translation during cell fate determination. Dysregulation of PUS7-deployed tdR networks is linked functionally to aberrant protein synthesis programs associated with hematopoietic stem cell (HSC) dysfunction and leukemogenesis in humans.[10] This work provided a paradigm shift for PUS-induced epitranscriptomic control of tdR biogenesis and function in stem cells. Additionally, tdRs are emerging signaling molecules in extracellular communications, which differentially affect the function of hematopoietic cell populations within the bone marrow niche and upon infection.[11,12] Beyond their roles in translation and hematopoiesis, tdRs have emerged as versatile molecules that shape the cellular response to stress through transcriptional and post-transcriptional effects, owing many additional regulatory functions in gene silencing, transcription, transgenerational inheritance of metabolic traits, and control of endogenous retroviruses (ERVs).[12] ERVs are highly mobile repetitive elements that retain the ability to retrotranspose and contribute to a significant portion of the cellular transcriptome,[13–15] underscoring their importance during embryonic development, aging, and various diseases.[16–19] Indeed, ERVs represent a significant source of cytosolic nucleic acids, including double-stranded (ds)RNAs and RNA-DNA hybrids, that can elicit strong inflammatory responses through the activation of intracellular pattern recognition receptors (PRRs).[16,20] Based on these findings, we hypothesized that PUS-mediated rewiring of tdR pools might enable rapid molecular adaptations to cell-intrinsic and -extrinsic cues shaping tissue homeostasis upon pathophysiological stress conditions.

Recent studies suggest that aging-associated expression of the Ψ synthase PUS10 may contribute to the functional decline of mouse HSCs.[21] Additional results using human cells revealed distinct roles of PUS10 in TRAIL-induced apoptosis,[22] microRNA (miRNA) biogenesis, and tRNA pseudouridylation, underscoring the contribution of its catalytic activity for cell growth.[23] Notably, meta-analysis pinpointed *PUS10* as a high-risk locus for Crohn's and celiac diseases,[24] suggesting a potential involvement in human inflammatory diseases. In this study, we define an unanticipated function for PUS10 as an essential gatekeeper of viral mimicry, which involves molecular regulation by distinct tdR subsets. Genetic loss of *Pus10* contributes to retrotransposable element (TE) dysregulation and ensuing inflammation, mediated by the accumulation of RNA-DNA hybrids, which may activate the cyclic GMP-AMP synthase (cGAS)-stimulator of interferon gene (STING) sensing pathway.[25] Similarly, impairments in Pus10 and TE alter the HSC response to inflammatory stress *in vivo*. Finally, our survey in humans delineates unanticipated correlations between PUS10 dysfunction and common autoimmune disorders. These studies underscore PUS10 and tdRs as crucial modulators of the viral mimicry response.

RESULTS

Pus10 depletion boosts the antiviral response without affecting murine development

Despite recent efforts,[21–23] the role of PUS enzymes and Ψ in mammalian development remains largely unresolved. Building on evidence that PUS10 dysregulation may contribute to aging and disease in mice and humans,[21,24,26] we sought to determine the pathophysiological consequences of its dysfunction *in vivo.* To this end, we generated whole-body *Pus10* knockout (KO) mice, hereafter denoted *Pus10KO,* using mouse embryonic stem cells (mESC) carrying a gene trap in intron four (Figure 1A). Leveraging a newly developed specific antibody that selectively recognizes the C-terminal region of the ~60-kDa mouse and human protein, we found widespread Pus10 expression across different tissues, including the liver, spleen, lung, and thymus, which was lost upon *Pus10* deletion (Figures 1A and 1B). *Pus10KO* mice were viable, fertile, born at the expected Mendelian rate, and did not present any overt morphological abnormalities affecting embryogenesis and the median animal lifespan (Figures 1A–1C and S1A), suggesting more specialized functions for *Pus10* in organismal physiology.

Unexpectedly, transcriptomic analysis of immortalized *Pus10KO* mouse embryonic fibroblasts (MEFs) revealed a striking upregulation of mRNAs enriched for interferon-stimulated genes (ISGs) (Figures 1A, 1D–1F, and S1B; Table S1), which were also noticeable in other cell types from *Pus10KO* mice (Figure S1C). In accordance, the increase in ISG expression was accompanied by resistance to lentiviral transduction and mild proliferative alterations compared with littermate control-derived *wild-type* (*WT*) cells (Figures S1D and S1E). Of note, reintroducing inducible FLAG-tagged Pus10 WT and its catalytically inactive (D342A) mutant allele[27] led to a similar transient normalization of aberrant ISG expression (Figures 1G and S1F), indicating that the Ψ synthase function is likely dispensable for the inflammatory phenotype in Pus10-deficient cells.

Pus10 depletion perturbs the levels of specific tRNA-derived small RNA subsets

PUS10 belongs to the sixth PUS family present only in Archaea and Eukarya and catalyzes modifications Ψ54 and Ψ55 in the T-loop of cytoplasmic tRNA subsets, corresponding to its consensus motif GUUCRANYC with the target uridine (U).[27,28] Nevertheless, a comprehensive analysis of the PUS10-RNA regulon in mammalian cells is lacking. Hence, we undertook individual-nucleotide resolution UV cross-linking and immunoprecipitation followed by high-throughput sequencing (iCLIP-seq)[29] to examine the genome-wide Pus10-RNA interactions at a single-nucleotide resolution in MEFs, using a specific anti-mouse Pus10 antibody. *Pus10KO* cells were used as a control to

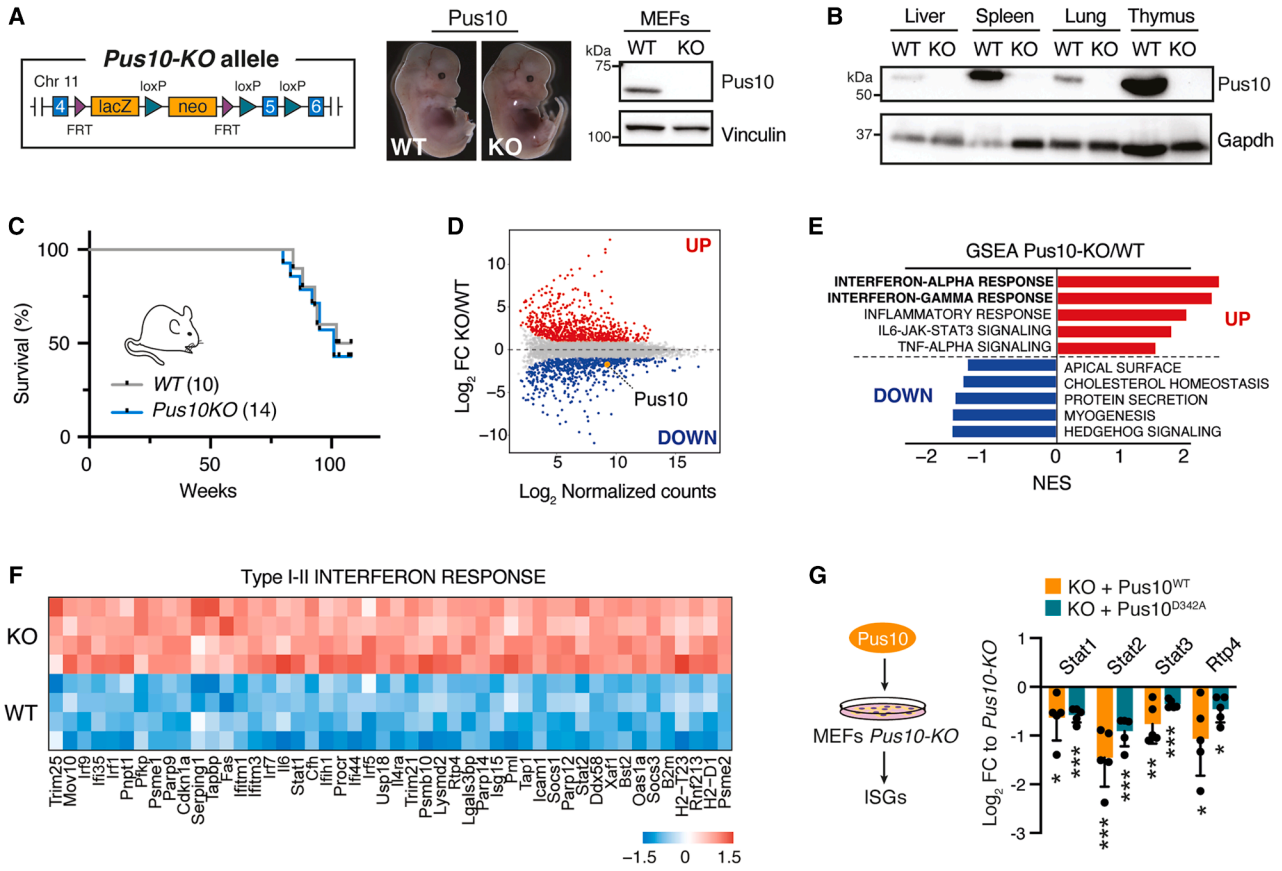

Figure 1. Pus10 depletion induces cell-intrinsic inflammation

(A) Left, schematic of the *Pus10KO* allele. Middle, representative images of embryos at embryonic day 13.5 (E13.5) illustrate no obvious developmental defects upon Pus10 genetic loss. Right, Pus10 protein analysis in *WT* and *Pus10KO* MEFs.

(B) Representative Pus10 protein analysis in different tissues for 11- to 14-week-old *WT* and *Pus10KO* littermates.

(C) Kaplan-Meier curve shows no differences in survival between *WT* and *Pus10KO* mice. The number of animals in each arm is indicated in the graph.

(D) Transcriptomic analysis of *WT* and *Pus10KO* cells. Graph shows differentially expressed transcripts as $\log_2$ fold change (FC) KO over WT normalized to mRNA abundance in four independent experiments. Upregulated and downregulated genes are shown in red ($\log_2$ FC > 1) and blue ($\log_2$ FC < −1), respectively. FDR <0.05.

(E) Gene set enrichment analysis (GSEA) reveals significant enrichments for inflammation-associated transcriptional programs in *Pus10KO* cells.

(F) Heatmap shows increased expression of interferon-stimulated genes (ISGs) in *Pus10KO* cells. Color bar indicates *Z* score transformation of normalized gene expression.

(G) Add-back of Pus10 or its catalytic inactive D342A mutant normalizes ISG expression. Graph shows mean $\log_2$ FC relative expression ±SD in *Pus10KO* cells ± $Pus10^{WT}$ (green) and $Pus10^{D342A}$ (orange) in five independent experiments. ***$p < 0.001$; **$p < 0.01$; *$p < 0.05$ (t test).

exclude non-specific RNA binding. This approach revealed a PUS10-specific RNA interactome overly dominated by tRNAs, highlighting binding to distinct tRNA isoacceptors (Figures 2A–2C and S2A). By extension, we delineated additional Pus10 interactions with spliceosomal RNAs (snRNAs), snoRNAs, long non-coding RNAs (lncRNAs), mRNAs, and microRNAs (miRNAs) (Figure 2A; Table S2). Peak analysis defined a putative Pus10 RNA consensus binding motif [GTTCRADNC], identified on tRNAs and other RNA species bound by Pus10 (Figures 2B and S2B).

Next, we reasoned that specific defects in Pus10-interacting RNA substrates might account for the innate inflammatory response observed in *Pus10KO* cells. Because of the extensive binding revealed by iCLIP-seq, we initially performed a comprehensive analysis of tRNA abundance without observing significant differences in isoacceptor levels, consistent with previous studies (Figure S2A).[23] Accumulating evidence indicates that tRNA fragmentation may provide an additional layer of gene regulation, expanding tRNA cellular functions.[12] Of note, accumulation of tdRs occurs at low levels and is mostly uncoupled from declines in full-length tRNA pools.[9,31–34] We hypothesized that Pus10 dysfunction might induce the accumulation of tdRs in the absence of global mature tRNA perturbations, similar to other tRNA-modifying enzymes.[9,33,34] Taking advantage of small RNA sequencing, we applied a well-established pipeline[30] to chart tRNA fragmentation events in Pus10-depleted cells (Figure 2D). Our analysis uncovered remarkable changes in the levels of distinct tdR categories, highlighting significant

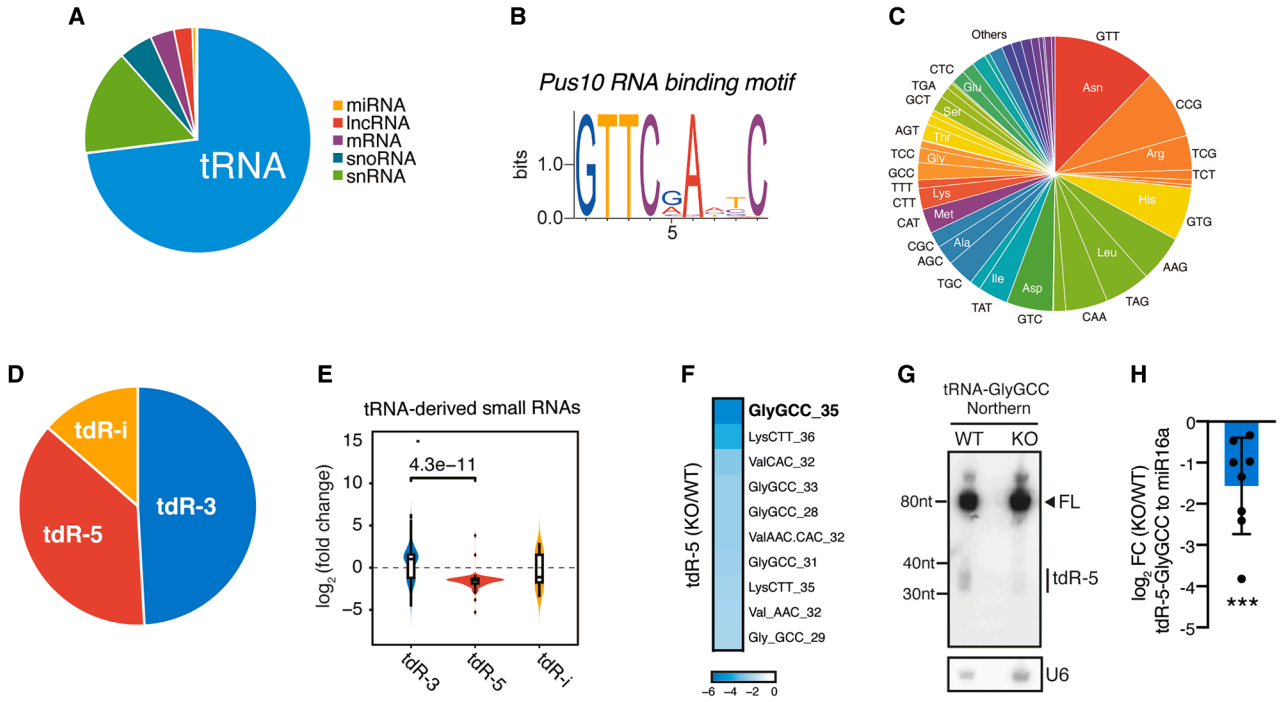

Figure 2. Pus10 modulates the accumulation of distinct tdRs

(A) Pie chart shows Pus10-RNA interactions in MEFs determined by iCLIP-seq.

(B) Sequence analysis of Pus10-specific iCLIP products defines a putative Pus10-RNA binding motif.

(C) Pie chart illustrates the enrichment of individual Pus10-bound tRNAs normalized to their abundance in MEFs determined by small RNA sequencing (smRNA)-seq.

(D) Pie chart shows the main categories of tdRs differentially expressed in *Pus10KO* cells. tdR-5 and tdR-3 denote 5′- and 3′-derived tdRs, respectively. tdR-i defines internally derived tdRs. tdR classification is based on the MINTMap.[30]

(E) Violin plot shows the mean difference (*Pus10KO* to *WT*) in normalized counts for each tdR measured by smRNA-seq.

(F) Heatmap shows the top 10 significantly downregulated 5′ tRNA-derived small RNAs (tdR-5s) in *Pus10KO* cells. FDR <0.01 tdR-5-GlyGCC (35 nt) is highlighted as the most downregulated tdR-5.

(G) Representative northern blot shows reduced accumulation of tdR-GlyGCC fractions in total RNA from *Pus10KO* compared with *WT* cells. The size of full-length (FL) tRNA-GlyGCC and corresponding fragments (tdR-5) is indicated. U6 levels are shown as loading control.

(H) Graph shows $\log_2$ FC (*Pus10KO*/*WT*) tdR-5-GlyGCC levels ±SD determined by stem-loop (SL) qPCR. ***$p < 0.001$ (t test).

reductions of fragments arising from the 5′-end of specific tRNA cognates (tdR-5), including those bound by Pus10 such as tRNA-ValCAC/AAC, tRNA-GlyGCC, and tRNA-LysCTT (Figures 2E and 2F). Among these alterations, 5′ tRNA-halves (35 nt), hereafter tdR-5-GlyGCC, emerged as the most downregulated tdR-5 species in *Pus10KO* cells (Figure 2E). This molecular defect was thoroughly validated using orthogonal approaches such as northern blot and stem-loop-based quantitative PCR (SL-qPCR) (Figures 2G and 2H).[9] By extension, we examined other RNAs identified by iCLIP-seq but did not observe major changes in the levels of Pus10-interacting mRNAs, snRNAs, snoRNAs, and miRNAs (Tables S2 and S3). Specifically, we observed differential expression of ∼70 miRNAs in *Pus10KO* cells, which were not detected by iCLIP and may be consistent with a putative role in pre-miRNA biogenesis described in human cells (Table S3).[23] However, only three miRNAs were predicted to target genes (Isg15, Ifit3, and Irf9) associated with the interferon (IFN)-alpha response (Table S3). Collectively, these results pinpointed tdR-5 depletion as a prominent molecular defect downstream of Pus10 dysfunction, which prompted further investigation into the contribution of these small RNAs toward cell-intrinsic inflammatory phenotypes.

Pus10 and tdR dysfunctions are associated with translation alterations and mis-expression of endogenous retrotransposons

Converging evidence in different systems indicated that tdRs are critically involved in the modulation of mRNA translation in response to pathophysiological stress through diverse mechanisms.[12] Consistent with our previous work pointing to a role for PUS proteins in tdR regulation and translation control,[9,10] we observed a remarkable increase of *de novo* protein synthesis rates in *Pus10KO* cells, as measured by the incorporation of radiolabeled methionine and cysteine (Figure 3A). Next, we sequenced actively translated polysomal mRNAs and calculated translation efficiency, a metric defined as ribosome occupancy per transcript normalized to total transcript abundance. As expected, we observed that translation efficiency was significantly higher in *Pus10KO* cells compared with WT cells (Figure 3B). Furthermore, we observe elevated translation levels of multiple

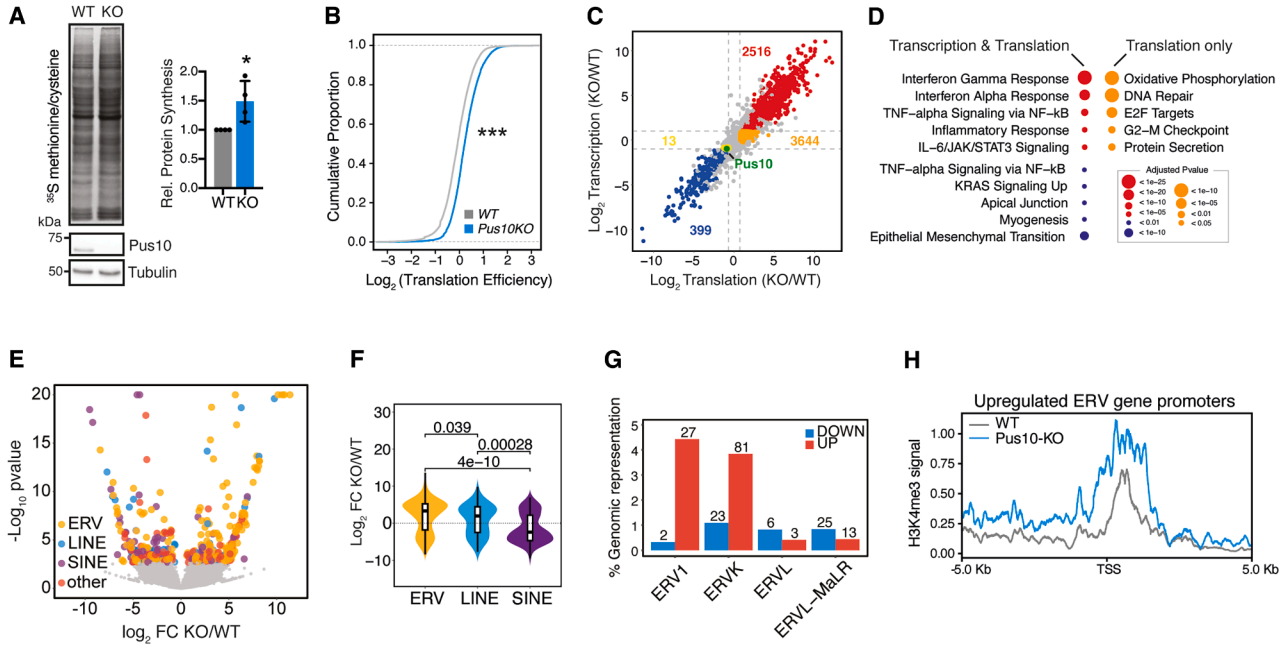

Figure 3. Pus10 loss perturbs translation and the expression of the endogenous virome

(A) Pus10 dysfunction enhances translation. Representative analysis of *de novo* protein synthesis in *WT* and *Pus10KO* cells using [^{35}S]-methionine/cysteine incorporation. Graph shows quantification of *de novo* protein synthesis ± SD in three independent experiments. *$p < 0.05$ (t test).

(B) Cumulative distribution of log2 translation efficiency in *WT* and *Pus10KO* cells. ***$p < 2.2 \times 10^{-16}$ (Wilcoxon signed-rank test).

(C) Graph illustrates $\log_2$ FC transcription (total RNA) and translation (polysomal mRNA) for each gene from three independent experiments. Transcripts undergoing both transcriptional ($|\log_2 FC| > 1$; FDR <0.05) and translational ($|\log_2 FC| > 0.7$; FDR <0.05) co-regulation are highlighted in red and blue, respectively. Translationally controlled mRNAs ($|\log_2 FC| > 0.7$; FDR <0.05) are shown in orange and yellow.

(D) Gene ontology (GO) analysis reveals significant enrichment of co-regulated transcriptional and translational terms, alongside translationally controlled gene programs.

(E) Volcano plot shows differentially expressed retrotransposons (TE). Different types are highlighted. $|\log_2 FC| > 1.5$; FDR <0.05.

(F) Violin plot shows the mean difference $\log_2$ FC KO/WT of endogenous retroviruses (ERV), long-interspersed nuclear elements (LINE), and short-interspersed nuclear elements (SINE) differentially expressed in *Pus10KO* cells. *p* value is shown (Wilcoxon test).

(G) Graph illustrates the absolute number of up- and downregulated ERVs belonging to the different classes. The percentage of ERVs relative to their genomic representation is shown.

(H) CUT&RUN signal enrichment of H3K4me3 over the promoter region of transcriptionally upregulated ERV genes in *Pus10KO* compared to *WT* cells.

inflammatory pathways, including type I-II IFNs and tumor necrosis factor (TNF)-alpha, alongside repression of developmental processes, consistent with their transcriptional upregulation and downregulation, respectively (Figures 3C and 3D; Table S4). Interestingly, our unbiased profiling delineated a selective enrichment for translation-based mRNA signatures, uncoupled from transcription, encoding metabolic programs associated with oxidative phosphorylation, DNA repair, proliferation, and G2/M checkpoint regulation (Figure 3D)—pathways that may reflect molecular adaptations associated with the autoinflammatory response in Pus10-deficient cells.[35,36]

Seminal work illustrated a critical contribution of tdRs in regulating multiple steps of ERV's life cycle.[37–39] Thus, we sought to determine whether Pus10 dysfunction altered retrotransposon expression and triggered inflammation. Using a dedicated bioinformatic pipeline to examine transcriptomic data from *Pus10KO* cells, we determined TE expression based on multiple and unique mapping to the mouse genome.[40] This analysis uncovered widespread perturbations affecting many TEs, including ERVs, long-interspersed nuclear elements (LINEs), and short-interspersed nuclear elements (SINEs) (Figures 3E and 3F; Table S1). There was a remarkable global increase in several ERVs belonging to the ERV1 and ERVK sub-families (Figure 3G), an upregulation of LINEs, including LINE-1 (L1), and there was an overall downregulation of the SINE B2 family (Figures S2C and S2D). The analysis of ERV divergence from the consensus sequence indicated that differentially expressed ERVs in *Pus10KO* cells were relatively "younger" than the average, providing a proxy of the evolutionary age (Figure S2E). Furthermore, epigenomic profiling using CUT&RUN[41] corroborated our TE analysis, illustrating a consistent increase of H3K4me3 levels at the transcriptional start site (TSS) of TE upregulated in *Pus10KO* cells (Figures 3H and S3F; Table S5). These findings suggest that Pus10 dysregulation and TE de-repression may converge to elicit a viral mimicry response.

Pus10-deficiency-induced RNA-DNA hybrids and cGAS-STING-driven inflammation

TE reactivation has been associated with the accumulation of cytosolic nucleic acids, such as double-stranded RNA (dsRNA)

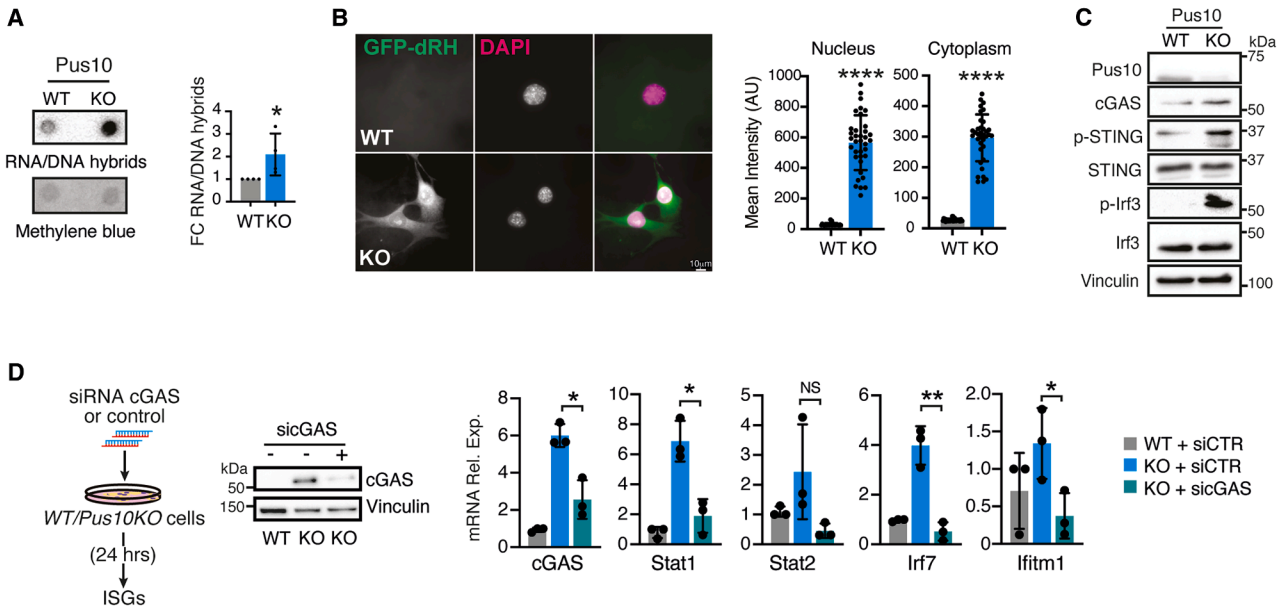

Figure 4. Pus10 deficiency promotes RNA-DNA hybrid accumulation

(A) Lack of Pus10 is associated with the accumulation of RNA-DNA hybrids. RNA dot plot shows increased reactivity to the RNA-DNA hybrid-specific S9.6 antibody in *Pus10KO* cells. Methylene blue staining is used as loading control. Graph shows mean levels of RNA-DNA hybrids relative to WT ± SD in four independent experiments. $p < 0.05$ (t test).

(B) Immunofluorescence analysis shows significant accumulation of RNA-DNA hybrids in the nucleus and cytoplasm of *Pus10KO* cells. Representative images of *WT* and *Pus10KO* cells stained with the recombinant GFP-dRH protein, which selectively binds RNA-DNA hybrids.[44] DAPI stains nuclei. Right, graphs show mean quantification of GFP-dRH nuclear and cytoplasmic intensity ±SD in *WT* and *Pus10KO* cells. Scale bar is 10 μm ****$p < 0.0001$ (t test).

(C) Protein analysis shows robust activation of the proinflammatory cGAS-STING signaling pathway in *Pus10KO* cells.

(D) cGAS downregulation normalizes ISG expression in *Pus10KO* cells. Left, representative cGAS protein analysis decreased levels upon transfection of an siRNA pool targeting cGAS (sicGAS) in *Pus10KO* cells. Right, graphs show mean relative mRNA expression ±SD of cGAS and four ISGs in *Pus10KO* cells transfected with non-targeting control (siCTR) or cGAS-specific siRNA pools in three independent experiments. **$p < 0.01$; *$p < 0.05$; NS, no statistical significance (t test).

and RNA-DNA hybrids, which trigger RNA and DNA sensing pathways eliciting inflammatory responses.[16,20] Following this premise, we used specific antibodies recognizing immunostimulatory nucleic acid forms to examine dsRNAs and RNA-DNA hybrids levels in *WT* and *Pus10KO* cells. No detectable changes in dsRNA levels and activation of RIG-I-like receptors (RLR), which mediate RNA sensing, were observed using RIG-I and MDA5 reporter cells[42] (Figures S3A and S3B). This was consistent with findings that downregulation of the essential adapter protein MAVS,[43] acting downstream of RLRs, did not restore ISG expression in *Pus10KO* cells (Figure S3C). Intriguingly, our analysis delineated a drastic increase of RNA-DNA hybrids highly specific to Pus10-depleted cells (Figures 4A and S3D). These molecular alterations were further validated through cellular fraction and immunofluorescence using a catalytic deficient human RNase H1 tagged with GPF, GFP-dRH.[44] This revealed remarkable RNA-DNA hybrids accumulation in the nucleus and cytoplasm of *Pus10KO* cells (Figures 4B and S3E), suggesting their role in Pus10-associated inflammation. Indeed, evidence suggests that RNA-DNA hybrids are sensed by the cGAS-STING signaling pathway,[25,45] converging on the downstream phosphorylation and activation of the interferon regulatory factor 3 (Irf3) with subsequent induction of ISG transcription. Accordingly, there was a marked upregulation of cGAS-STING pathway activation, as shown by an increase in phosphorylated Irf3 (p-Irf3) in *Pus10*-depleted cells (Figure 4C). This activation could be partly blunted by overexpression of RNase H1 and by treatment with the reverse transcriptase inhibitor lamivudine (3TC) (Figures S3F and S3G). Moreover, ISG expression could be normalized upon partial knockdown of cGAS and upon treatment with the STING inhibitor H-151, STINGi, in these cells[46] (Figures 4D and S3H), further establishing a role for cGAS-STING in sensing RNA-DNA hybrids downstream in *Pus10KO* cells.

tdR-5-GlyGCC counteracts increased cGAS-STING signaling in *Pus10KO* cells

Motivated by our results and prior studies illustrating a role for similar 5′ tRNA-halves in repressing TE expression during development,[37,38] we asked whether the pronounced reductions of tdR-5-GlyGCC upon Pus10 depletion contributed to the viral mimicry in MEFs. Significantly, transduction of synthetic tdR-5-GlyGCC oligos in *Pus10KO* cells readily restored the levels of RNA-DNA hybrids and p-Irf3 to homeostatic conditions without changes in viability and global translation (Figures 5A–5C and S4A–S4C). These effects were specific to tdR-5-GlyGCC as treatment with other tdR-5s, including a 35-nt scramble control oligo (tdR-5-CTR) and tdR-5-LysCTT, did not rescue the defects (Figure S3D). Notably, tdR-5-GlyGCC supplementation selectively normalized the expression of ERV sub-families that were among the most upregulated in *Pus10KO* cells, including ERV1

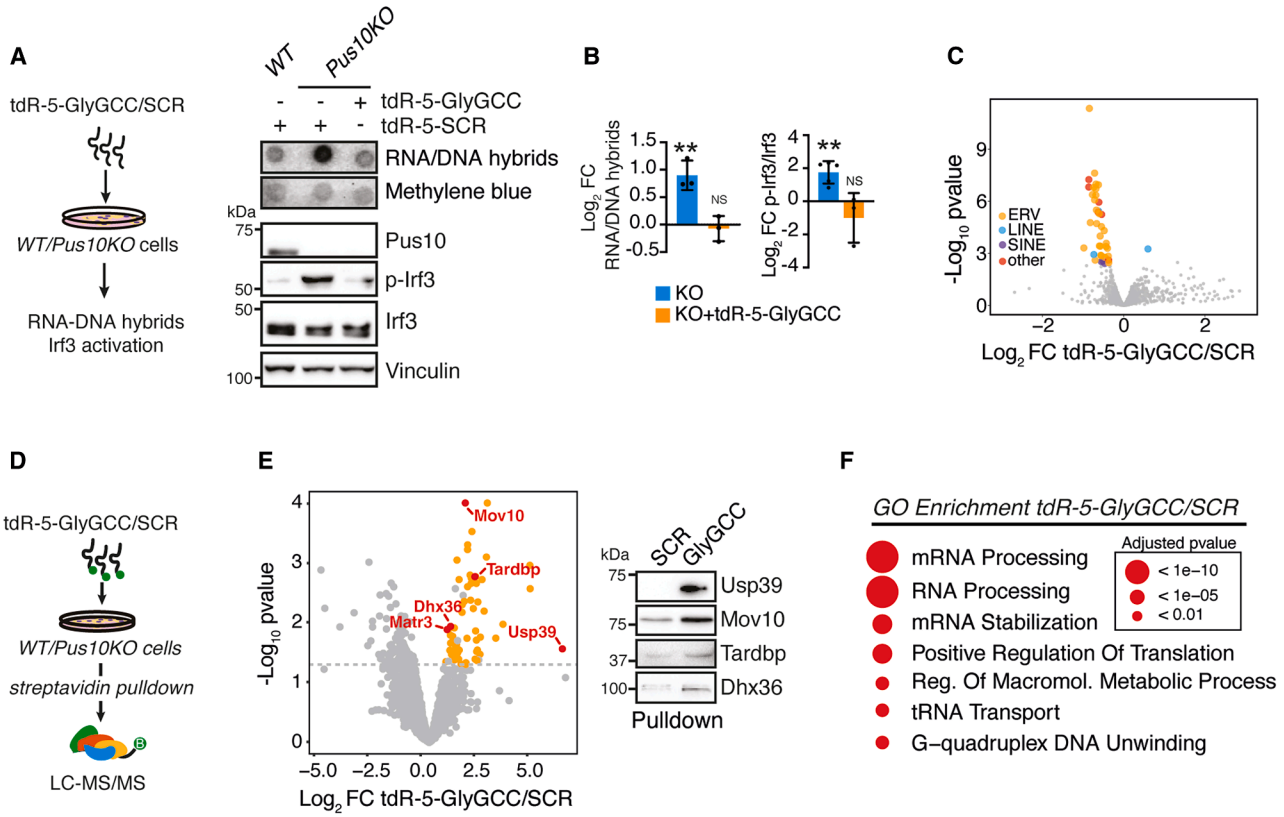

Figure 5. tdR-5-GlyGCC modulates inflammation downstream of Pus10 loss

(A) Transduction with tdR-5-GlyGCC rescues RNA-DNA hybrid accumulation and subsequent cGAS-STING pathway activation in *Pus10KO* cells.

(B) Left, graph shows $\log_2$ FC RNA-DNA hybrid levels detected by anti-S9.6 antibody staining normalized to WT ± SD in *Pus10KO* cells with or without transfection of tdR-5-GlyGCC (20 nM) in three independent experiments. Methylene blue staining is used as loading control. Right, graph shows mean phosphorylated over total Irf3 levels in *Pus10KO* normalized to *WT* cells ±SD 24 h post-transfection with transfection of tdR-5-GlyGCC (20 nM) or tdR-5-scramble control oligo (SCR) in at least three independent experiments. $^{**}p < 0.01$; NS, no statistical significance (one-way ANOVA).

(C) Volcano plot shows $\log_2$ FC differentially expressed retrotransposons in *Pus10KO* cells transfected with tdR-5-GlyGCC or tdR-5-SCR. FDR <0.05.

(D) Schematic depicts the quantitative, unbiased approach employed to identify protein complexes bound to 3′-biotinylated tdR-5-GlyGCC in *Pus10KO* cells.

(E) Volcano plot showing significantly enriched proteins (orange) in tdR-5-GlyGCC compared with control tdR-5-SCR pull-downs in four independent experiments ($\log_2$ FC > 0.75; $p < 0.05$). Significant interactions relevant to inflammation and TE regulation are highlighted in red. Right, representative western blot showing enrichment of Usp39, Tardbp, Mov10, and Dhx36 in tdR-5-GlyGCC compared with SCR pull-downs.

(F) Gene ontology analysis of biological processes enriched for proteins binding tdR-5-GlyGCC.

(MuLV, RLTR4) and ERVK (IAPEZ, MMETn, IAPLTR1, RLTR13G) elements (Figure 5C; Table S1). Furthermore, tdR-5-GlyGCC restored ISG upregulation induced by siRNA-mediated PUS10 downregulation in cGAS-STING-competent human fibroblasts[47] (Figure S4E), pinpointing a conserved role in directing cell-intrinsic inflammatory signals. To dissect the mechanism by which tdR-5-GlyGCC modulates inflammation, we performed quantitative proteomics by transducing biotinylated tdR-5-GlyGCC in *Pus10KO* and *WT* cells (Figure 5D). This approach revealed a significant enrichment for RNA processing factors in tdR-5-GlyGCC pull-downs compared with a scramble tdR-5 control (SCR) sequence (Figures 5E and 5F; Table S6), including Usp39, Dhx36, Tardbp, Mov10, and Matr3. These factors play key roles in inflammation by impacting the JAK/STAT, NF-kB, and cGAS-signaling pathways, as well as directly modulating TE activity.[48–51] This suggests that Pus10 and tdR-5-GlyGCC contribute to a multilayered regulatory network that broadly modulates inflammation.

Pus10 alters hematopoietic stem cell response to inflammatory stress

HSCs are exquisitely sensitive to TE perturbations, which drive genomic instability and critically integrate inflammatory cues to adapt the hematopoietic response.[52–54] Indeed, under stress requiring hematopoietic regeneration, TE expression is increased in HSCs, promoting an inflammatory milieu needed to exit quiescence, as we and others have suggested.[55,56] Hence, we examined Pus10 contribution to immune responses in HSCs under homeostasis and following stress conditions. In agreement with a recent study illustrating that loss of *Pus10* led to mild alterations of hematopoietic homeostasis,[21] we did not observe significant differences in the frequencies of bone marrow (BM)-derived hematopoietic stem and progenitor cells (HSPCs), including HSCs, multipotent (MPP), and granulocyte-monocyte-lymphoid progenitors (GMLPs), in 5- to 7-month-old *Pus10KO* mice compared with *WT* littermates (Figures S5A

and S5B). Likewise, the percentage of lymphoid and myeloid cells in the peripheral blood (PB) and other blood parameters of these animals were not altered (Figures S5C–S5E). To delve further into underlying molecular defects in HSCs, we performed transcriptomic analysis of Lineage-Sca-1+cKit+ (LSK), from 3-month-old *Pus10KO* mice. This revealed upregulation of cell cycle- and metabolic activation-related terms related to E2F, MYC, oxidative phosphorylation, and proliferation but also an enrichment for IFN-alpha and -gamma signaling in *Pus10KO* HSPCs compared with *WT* controls independent of changes in Sca1+ expression levels (Figures 6A, 6B, and S6A; Table S7). We also noticed a downregulation of terms associated with TNF-alpha and TGF-beta, suggesting additional perturbations involving other inflammatory signaling pathways. Interestingly, the transcriptional alterations observed in *Pus10KO* LSK cells were associated with the activation of distinct ERVs (Figure 6C), prompting further investigation into the inflammatory response of these cells.

Based on these findings and evidence that TE expression is induced in HSCs upon stress demanding hematopoietic reconstitution,[55,56] we next sought to challenge HSC self-renewal and repopulation capacity *in vivo.* We performed competitive whole BM transplantation (BMT) into sub-lethally irradiated recipients, a procedure that imposes proliferative and inflammatory stress (Figure 6D).[57,58] Analysis of *Pus10KO* chimeras revealed a consistent trend for higher donor reconstitution, which was particularly pronounced at four weeks post-transplantation (Figures 6E, S6B, and S6C), prompting a putative function of Pus10 in hematopoiesis during stress. To further characterize the immune responses in *Pus10KO* HSCs, we examined how Pus10 loss affected HSC behavior following acute inflammatory cues *in vivo*. To this end, we serially injected *WT* and *Pus10KO* mice with polyinosinic:polycytidylic acid (poly I:C), a synthetic dsRNA analogue that mimics viral infection, and performed competitive whole BMT (Figure 6D). Accordingly, BM analysis of *Pus10KO* transplanted mice revealed an expansion in the frequencies of several HSPC populations, including HSCs, MPPs, GMLPs, and common lymphoid progenitors (CLPs) (Figure 6G). Analysis of *Pus10* chimeras revealed a robust multilineage engraftment in *Pus10KO* chimeras up to 16 weeks post-transplantation (Figure 6H). In contrast, *WT* chimerism was drastically impaired, consistent with previous studies indicating that poly I:C treatment hampers HSC long-term potential through IFN-alpha induction.[59] Of note, a transient increase in engraftment was also noticed at four and eight weeks post-transplantation in a cohort of secondary *Pus10KO* recipient grafts (Figure S6D), suggesting that Pus10 depletion modulates long-term HSC function upon treatment with poly I:C. These data indicate that Pus10 dysregulation may enhance HSC tolerance to inflammatory stress.

Impaired PUS10 activity correlates with human autoimmune disorders

A wealth of studies has revealed the contribution of host DNA and RNA in triggering aberrant activation of inflammatory signaling in the etiology of various autoinflammatory diseases.[60] A notable example is the pathogenic activation of type I IFNs in systemic lupus erythematosus (SLE), a chronic inflammatory disorder characterized by a range of clinical features, including multiorgan tissue damage, such as skin, joints, brain, kidney, lung, and blood vessels.[61,62] Hence, we sought to broaden our results and explore the PUS10's role in autoimmune conditions. To this end, we developed a specific molecular gene signature (GS) consisting of ~2,500 differentially expressed genes in *Pus10KO* MEFs (Figure 7A; Table S1), which provides a robust matrix to assess PUS10 protein function across different patient datasets. By leveraging the specific PUS10 molecular fingerprint, we uncovered a significant reduction of PUS10 activity in a published cohort of SLE patients[63] (Figure 7B). There was a positive correlation between a published SLE-GS and genes upregulated in *Pus10KO* cells, which was further corroborated by the analysis of single-cell (sc) expression profiles in these patients (Figures 7C and 7D). Accordingly, we observed that PUS10 and IFN-alpha gene signatures inversely correlated in SLE patients (Figure S7A). Consistent with meta-analysis indicating PUS10 as a risk locus for Crohn's disease (CD),[24] PUS10-GS score was markedly reduced in CD and ulcerative colitis (UC) patients (Figure 7E),[64] common inflammatory bowel diseases (IBD), which displayed inflammation-related molecular responses, corresponding to type I-II IFNs and TNF-alpha (Figure S7B). Our analysis revealed a marked inverse correlation between PUS10 and IFN-alpha molecular signatures in CD patients (Figure S7C), supporting our analysis that PUS10 activity was reduced in this cohort. To validate PUS10-GS analysis in IBD, we measured PUS10 mRNA and protein levels directly in colon biopsies from small CD and UC patient cohorts (Table S8). This demonstrated PUS10 reductions, particularly marked in UC specimens relative to healthy controls (HCs), which was accompanied by a trend toward lower tdR-Gly-5-GCC levels (Figure S7D) and a significant upregulation of interferon transmembrane proteins 1 and 3, IFITM1 and IFITM3, two ISGs overexpressed in PUS10-depleted murine and human cells[23] (Figures 7F and 7G). Building on these results and evidence that inflammation is associated with a higher risk of developing cancer in IBD, we surveyed a cohort of 98 colon cancer cases[65] and found a selective reduction of PUS10-GS score in the tumor specimens when compared with normal tissue from the same patients and 50 healthy donors (Figure 7H). To further investigate the contribution of PUS10 to IBD *in vivo*, we compared the susceptibility to colitis induced by dextran sulfate sodium (DSS), which recapitulates the features of human UC,[66] of *WT* and *Pus10KO* mice. These experiments demonstrated that Pus10 depletion affected the dynamic response to inflammation induced by low-dose DSS treatment, which minimally impacted WT mice but led to rapid and sustained weight loss in *Pus10KO* mice, accompanied by increased intestinal infiltration of neutrophils (Figures 7I–7K), immune cells centrally implicated in this colitis model.[66] Collectively, our findings suggest that PUS10 molecular dysfunction may be integral to the inflammatory process underlying certain human autoimmune conditions.

DISCUSSION

The underlying mechanisms linking RMP impairments to innate immunity are incompletely understood.[67] Here, we uncover PUS10, a Ψ synthase, as an unanticipated regulator of the innate

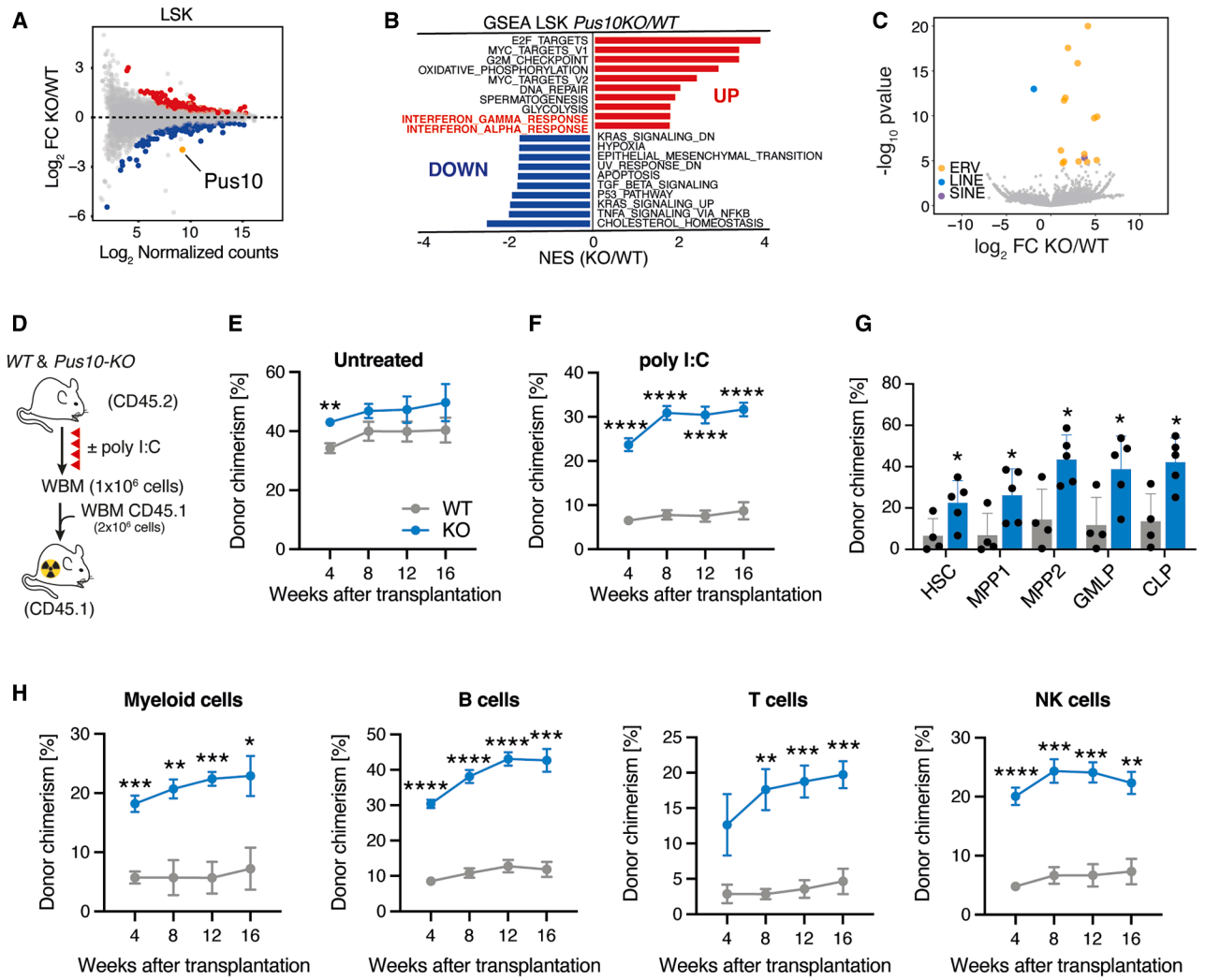

Figure 6. Pus10 impacts hematopoiesis upon pro-inflammatory stress *in vivo*

(A) Transcriptomic analysis of Lineage-Sca-1+c-Kit+ (LSK) cells isolated from *WT* ($n = 2$, male and female) and *Pus10KO* ($n = 2$, male and female) 10- to 14-week-old mice. Graph shows differentially expressed transcripts as $\log_2$ fold change (FC) KO over WT normalized to mRNA abundance. Upregulated and down-regulated genes are shown in red ($\log_2$ FC > 1) and blue ($\log_2$ FC < −1), respectively. FDR <0.05.

(B) GSEA reveals enrichment for IFN-alpha and -gamma signaling pathways (highlighted) in *Pus10KO* LSK cells.

(C) Volcano plot shows differentially expressed ERV, SINE, and LINE retrotransposons in *Pus10KO* LSK cells. $|\log_2 FC| > 1.5$; FDR <0.05.

(D) Loss of Pus10 alters hematopoietic stem cell and progenitors (HSPCs) response to inflammatory stimuli. Schematic illustrates the experimental setup used for the competitive bone marrow (BM) transplantation ± treatment with poly I:C, a synthetic dsRNA analogue serving as viral mimetic.

(E and F) Graph shows mean % donor chimerism (CD45.2+ cells) ± SEM in the peripheral blood (PB) of mice transplanted with 1×10^6 whole BM cells (CD45.2) from *WT* ($n = 4$) and *Pus10KO* ($n = 5$) mice subjected to serial injection ± poly I:C, a synthetic dsRNA analogue serving as viral mimetic. PB was analyzed every 4 weeks. ****$p < 0.0001$; **$p < 0.01$ (t test).

(G) Analysis of the hematopoietic progenitor compartment 16 weeks post-transplantation shows percentage donor chimerism (CD45.2) ± SD of HSC [LSK, CD150+CD48⁻CD201+], MPP1 (LSK, CD150-CD48⁻), MPP2 (LSK, CD150+CD48⁺), GMLP (LSK, CD150-CD48⁺), and CLP (LSK, CD127+CD135+) from poly I:C-treated *WT* ($n = 4$) and *Pus10KO* ($n = 5$) grafts. *$p < 0.05$ (t test).

(H) Graph shows mean percentage donor chimerism (CD45.2) ± SEM of myeloid (CD11b+), B (CD19⁺), T (CD3⁺), and NK (NK1.1+) cells in the peripheral blood (PB) of primary recipients transplanted with poly I:C-treated *WT* and *Pus10KO* WBM cells. Each group is four to five animals. ****$p < 0.0001$; ***$p < 0.001$; **$p < 0.01$; *$p < 0.05$ (t test).

immune response, driven at least in part by unrestricted ERV and LINE transposons activation. Critically, Pus10 deploys specific tdR subsets, including tdR-GlyGCC, as a line of defense against immunogenic RNA-DNA hybrids, which promote sterile inflammation, at least in part, through the cGAS-STING axis. Dysregulation of the molecular circuitry orchestrated by Pus10 mounts an antiviral response sustained by the type I-II IFN pathway, likely independent from its Ψ catalytic activity. This induces cellular anergy to proinflammatory stimuli, boosting HSPC self-renewal and multilineage differentiation capacity *in vivo*. Our

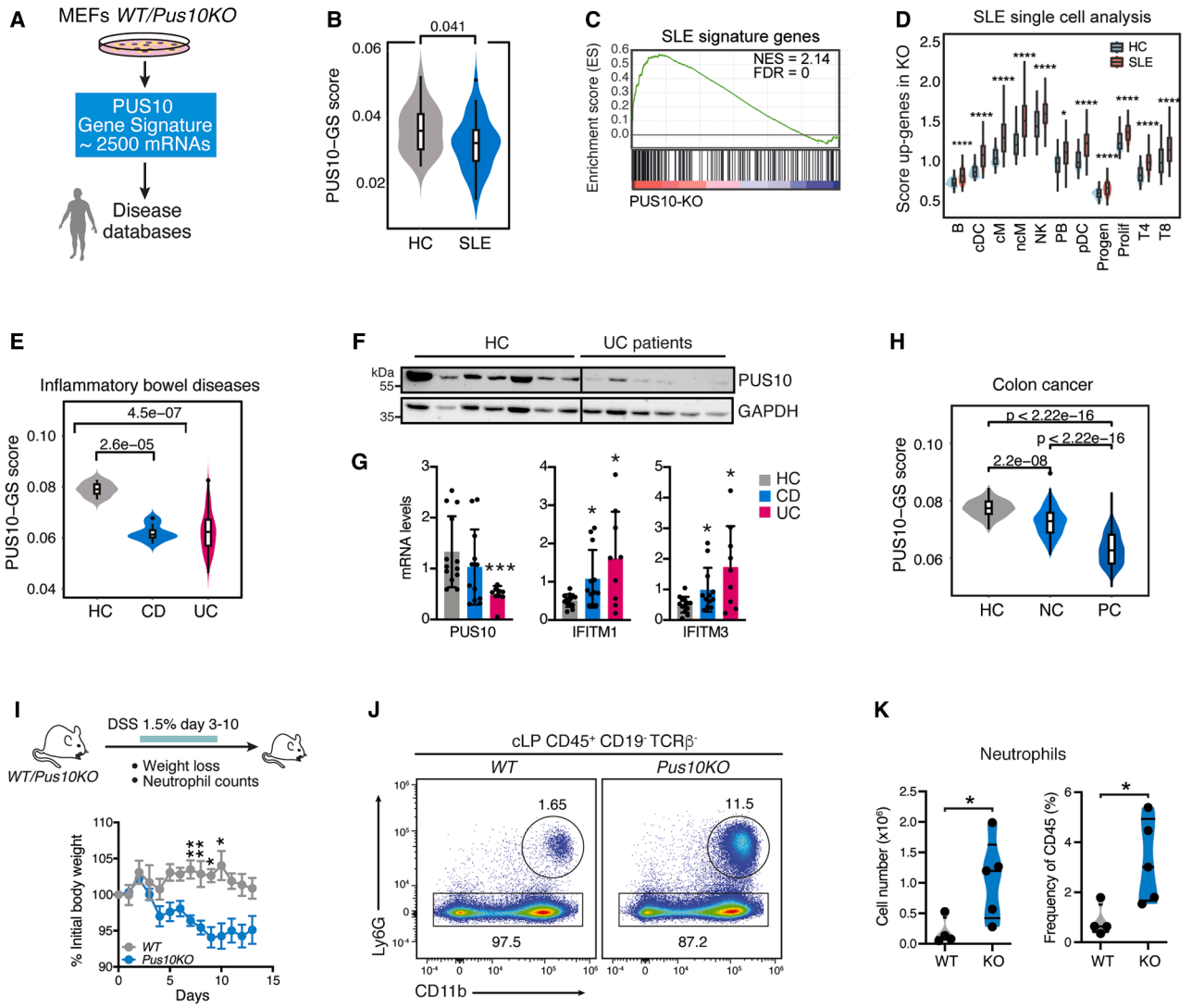

Figure 7. PUS10 dysfunction is associated with human autoimmune disorders

(A) Transcriptomic analysis of *Pus10KO* cells was used to build a Pus10-gene signature (GS) consisting of ~2500 differentially expressed genes (DEG), $|\log_2 FC| > 0.58$; FDR <0.05.

(B) Pus10-GS correlates with molecular gene expression patterns in systemic lupus erythematosus (SLE). HC denotes healthy control. *p* value is shown (Wilcoxon test).

(C) GSEA shows significant enrichment of the SLE-GS with genes upregulated in *PUS10KO* cells.

(D) Single-cell (sc) RNA-seq data analysis shows significant correlations between genes upregulated in *Pus10KO* cells and molecular profiles associated with distinct hematopoietic cell populations from SLE patients.

(E) Pus10-GS is significantly downregulated in inflammatory bowel conditions, such as Crohn's disease (CD) and ulcerative colitis (UC). *p* value is shown (Wilcoxon test).

(F) Representative protein analysis shows reduced PUS10 levels in intestinal biopsies from UC ($n = 6$) patients compared with HCs ($n = 7$).

(G) Graphs show mRNA levels ± SD of PUS10, IFITM1 and IFITM3 in HCs ($n = 13$), CD ($n = 12$), and UC patients ($n = 9$). ***$p < 0.001$; *$p < 0.05$ (t test).

(H) Pus10-GS is significantly downregulated in colon cancer specimens (PC) compared with HCs and normal colon (NC) tissues from the same patients. *p* value is shown (Wilcoxon test).

(I) Top, experimental design of the DSS-induced colitis model. Bottom, graph shows body weight ± SD of *WT* and *Pus10KO* mice untreated or treated with 1.5% DSS in one representative experiment. Each group is four and five animals. **$p < 0.01$; *$p < 0.05$ (ANOVA).

(J) Fluorescence-associated cell-sorting (FACS) plots showing the expression levels of the leukocyte-specific markers Ly6G and CD11b in the immune cell population (CD45+/CD19−/TCRβ−) from the colonic lamina propria (cLP) of *WT* and *Pus10KO* mice.

(K) Graphs indicating the mean number and frequency of neutrophils (Ly6G + CD11b+) ± SD in the cLP of *WT* ($n = 4$) and *Pus10KO* ($n = 5$) mice. *$p < 0.05$ (t test).

survey in humans underscores intriguing clinical correlations between PUS10 dysfunction and gene expression programs in autoimmune disorders, such as SLE and IBD, characterized by sustained levels of inflammation and increased risk of malignant transformation. Consistently, Pus10 loss enhances susceptibility to DSS-induced colitis, recapitulating the pathological features of human IBD. These findings provide important molecular insights into how PUS10 may train the innate immune system in mammals.

Accumulating evidence highlights essential roles for tdRs in adapting the cellular stress response to various cell-intrinsic and -extrinsic cues, providing additional layers to control genetic information.[12,68] Notably, prior work has established a central link between the dysregulation of tRNA-modifying enzymes and the accumulation of specific tdR subsets, which converge on protein translation to direct critical cellular transitions during development and tumorigenesis.[9,10,33,34] A striking example is PUS7, which deploys a class of tdR-5s, denoted mTOG, in a Ψ-dependent manner to steer protein synthesis and direct embryonic and hematopoietic stem cell differentiation.[9] In this study, we discovered that tdR-5-GlyGCC subsets are required to restrain cell-intrinsic inflammatory stress downstream of PUS10 loss. Previous findings indicate that similar tRNA-5-GlyGCC halves were enriched in sperm cells to epigenetically repress the murine endogenous retrovirus type-L (MERVL) during embryonic development.[37] Likewise, we show that tdR-5-GlyGCC halves may counteract de-repression of ERV elements and the accumulation of immunogenic RNA-DNA hybrids in *Pus10*-depleted cells through multiple interactions with RNA processing factors with established roles in inflammation and genome integrity. Striking examples include the deubiquitinase USP39, which modulates IFN signaling via STAT1 and nuclear factor (NF)-κB stabilization and is involved in DNA integrity.[50,51,69] Another example is the RNA/DNA-binding protein TARDBP, commonly associated with inflammation in neurodegenerative disorders and IBD and recently implicated in TE transcriptional deregulation linked to defects in R-loops and DNA modification.[70,71] Additionally, the RNA helicase MOV10 inhibits retrotransposon mobilization in somatic and germ cells.[72–74] Notably, TARDBP and MOV10 also exert antiviral immunity through the regulation of IRF3 independently of RLRs activation.[75,76] Nonetheless, future efforts are needed to fully elucidate the basis for TE de-repression by PUS10 and tdR dysfunctions. Given that tdRs can affect multiple steps of the TE life cycle through effects at the epigenetic, transcriptional, and post-transcriptional levels,[37,38,77] it is conceivable that combinatorial synergies may contribute to the molecular alterations associated with PUS10 deficiency. Although we could not find significant sequence homology between tdR-3 and TE altered in *Pus10KO* cells, it remains possible that different tdR pools may act synergistically to modulate the endogenous virome and cellular fitness downstream of Pus10. Interestingly, 5′ tRNA-5-GlyGCC halves form R-loop structures at their corresponding tRNA loci to avoid the formation of transcriptionally inhibitory long tRNA-DNA hybrids, ensuring tRNA expression during zebrafish development.[78] Thus, loss of tdR-5-GlyGCC may promote the accumulation of R-loops, providing additional substrates for activating cytosolic nucleic acid receptors, including cGAS and TLR3, as recently reported.[79] Evidence suggests that tdR biological activities involve complex molecular and structural arrangements, such as nicked tRNAs, tdR dimers, and tdR tetramers.[80–82] Notably, tdR-5s from Gly-GCC were shown to dimerize and accumulate as nicked tRNA forms in human cells, suggesting that multiple structures may be functionally involved in modulating inflammation.[80,83] RNA modifications, including Ψ and methylations, can provide additional regulatory layers affecting the function and structure of tdRs.[9,84] While tRNA-GlyGCC was not reported to be a direct substrate of PUS10 in human cells,[23] its methylation induced fragmentation in cancer cells.[85] As such, future work is required to elucidate the mechanisms by which PUS10 influences epitranscriptomic modifications and secondary structure of tdRs, as well as other abundant small RNAs it binds (e.g., snoRNAs and snRNAs), thereby fine-tuning their biogenesis and function during inflammation.

The innate immune response provides a first line of defense against pathogens and its dysregulation is often associated with autoimmune disorders.[86] Our analysis indicates that Pus10 loss does not affect embryogenesis and lifespan under steady-state conditions; however, its deletion promotes a viral mimicry that may shape the innate immune memory *in vitro* and *in vivo*. Pus10-depleted cells display increased resistance to viral infection, which is molecularly mediated by the activation of IFN inflammatory signaling. Interestingly, previous studies indicate that IFN stimulation improves antiviral protection, conferring a transcriptional memory, including several ISGs, that enables quicker responses upon restimulation in different cells.[87] Because IFN-induced transcriptional memory is associated with the acquisition of specific chromatin marks affecting the recruitment of RNA polymerase at IGSs, it is conceivable that the molecular perturbations induced by Pus10 deletion may modify the epigenome, enabling faster IFN activation upon stimulation. Our data suggest that the accumulation of RNA-DNA hybrids triggers the cGAS-STING axis to fuel the proinflammatory cascade in Pus10-depleted cells. However, additional work is required to definitively demonstrate that RNA-DNA hybrids co-localize with and drive cGAS activation in *Pus10KO* cells. Besides the accumulation of proinflammatory nucleic acids, TE expansion has been shown to directly affect the mammalian IFN regulatory network, likely due to an evolutionarily driven viral adaptation exploiting the host's immune signaling pathways.[88] Conceivably, additional TE-mediated perturbations of IFN-associated genes may alter the immune response, including HSC dysfunction, in *Pus10KO* animals. Although *Pus10* appears to be dispensable for long-term hematopoiesis under homeostatic conditions in mice, its depletion may establish a "tolerance" to acute stress induced by poly I:C treatment and BMT, requiring rapid HSC adaptations from quiescence to proliferation states. Our results support prior work indicating that while negligible TE levels are associated with quiescent HSCs,[89,90] TE expression is strongly induced in HSPCs upon chemotherapy, resulting in an inflammatory response that supports hematopoietic regeneration.[55]

Natural stress that occurs during aging has been linked to TE de-repression in human cells, which may contribute to the development of senescence phenotypes. These phenotypes are, at least partly, established through the activation of innate immune

signaling, notably by the cGAS-STING pathway.[16] These observations may be in line with findings that Pus10 is overexpressed in aged murine HSCs,[21] which may prompt a role for PUS10 in safeguarding genome integrity from age-associated TE de-repression and inflammation. A putative role for PUS10 in maintaining HSC function is further suggested by our findings that *Pus10KO* HSPCs displayed inflammatory gene signatures associated with aberrant ERV expression. Interestingly, aging is characterized by chronic low-grade inflammation,[16] a process that may favor the selection and expansion of mutant HSC clones in patients with clonal hematopoiesis of indeterminate potential (CHIP).[53] As such, it would be interesting to examine whether PUS10 dysfunction alters the inflammatory response driving adaptation to sustained levels of proinflammatory cues in CHIP patients, which are characterized by an increased frequency of hematological malignancies and other diseases. In keeping with this, our human survey indicates that reduced PUS10 activity correlates with inflammation in SLE and IBD, such as CD and UC, associated with a high risk of developing colon cancer.[91,92] It is tempting to speculate that PUS10 may coordinate the surveillance of the endogenous virome, thus modulating immune responses that impact tissue homeostasis vs. inflammatory states. This notion may be further supported by single-cell analysis delineating specific TE alterations in colonic epithelial cell subsets from CD patients,[93] and findings that ERV expression promotes microbiota-induced inflammation via the cGAS-STING axis, a mechanism required for host commensal specific immunity in the skin.[94] In this context, aberrant activation of the innate immune response upon PUS10 dysfunction may set the stage for the development of autoinflammatory conditions and malignant transformation, a hypothesis supported by our *in vivo* evidence showing that *Pus10KO* mice exhibit increased sensitivity to a chemically induced colitis model. As such, more studies are needed to elucidate how PUS10 contributes to immune alterations driving the evolution of autoimmune diseases. Collectively, our work uncovers PUS10 as an integral regulator of cell-intrinsic immune responses, which underscores a regulatory interface between epitranscriptome and innate immunity with potentially broad clinical implications for the etiology of human autoimmune disorders.

Limitations of the study

This study links PUS10 to autoinflammation through the regulation of specific tdR subsets, supporting a functional role of tdR-5-GlyGCC in this process. However, PUS10 dysfunction alters various tdR species without affecting tRNA levels, consistent with previous studies.[12] Hence, understanding how PUS10 influences tdR biogenesis to steer gene expression and shape immune responses remains an important future challenge. Our findings suggest that PUS10-associated tdR dysfunction promotes RNA-DNA hybrid accumulation, which may drive cGAS-STING activation, prompting the contribution for TE de-repression in autoinflammation. Nonetheless, further research is required to fully delineate how PUS10 orchestrates the crosstalk between TE and IFN-related pathways, and whether alternative mechanisms contribute downstream of PUS10 by activating cGAS and other pattern recognition receptors, as recently proposed.[79] Thus, a comprehensive genome-wide analysis of RNA-DNA hybrids is needed to define the repertoire of proinflammatory nucleic acids and their corresponding receptors in PUS10-depleted cells. Addressing these outstanding questions will advance our understanding of PUS10 gene regulatory roles during immune homeostasis and in the etiology of autoimmune diseases.

RESOURCE AVAILABILITY

Lead contact

Further information and requests should be directed to and will be fulfilled by the lead contact, Cristian Bellodi (cristian.bellodi@med.lu.se).

Materials availability

Commercially available reagents are listed in the key resources table. Plasmids generated in this study are available upon request from the lead contact with a completed materials transfer agreement.

Data and code availability

- Raw and analyzed sequencing data have been deposited at the Gene Expression Omnibus (GEO) database (https://www.ncbi.nlm.nih.gov/geo/) with the GEO: GSE248959. Deposited data are publicly available as of the date of publication.
- Proteomic data have been deposited to the ProteomeXchange Consortium via the PRIDE partner repository with the identifier, PRIDE: PXD061235.
- This paper does not report original code.
- Any additional information required to re-analyze the data reported in this paper is available from the lead contact upon request.

ACKNOWLEDGMENTS

We thank all the members of the Bellodi laboratory for helpful comments and J. Jakobsson for critical reading. We thank the Lund Stem Cell Center Flow Cytometry and Proteomics core facilities, J. Hansson, and M. Björklund for technical assistance. This work was supported by the Swedish Foundations' Starting Grant (SFSG) (C.B.), StemTherapy (C.B.), Swedish Research Council (Vetenskapsrådet) (C.B.), Swedish Cancer Society (Cancerfonden) (C.B.), Swedish Childhood Cancer Foundation (C.B.), Spanish Ministry of Science and Innovation grant PID2022-141124NB-I00 (A.C.-R.). P.S. is currently being supported by the DZNE and the Ministry of Culture and Science of the State of North Rhine-Westphalia (CANcer TARgeting, CANTAR program as part of Netzwerke 2021) and the National Hub for Nanobody Cancer Theranostics (THUNDER) from German Cancer Aid. Work in part related to the topic of this manuscript was supported by the Fru Berta Kamprad Foundation (C.B.), Swedish Childhood Cancer Fund (Barncancerfonden) (C.B), Helmholtz-Gemeinschaft Aging and Metabolic Programming (AMPro) Consortium (P. S.), and Worldwide Cancer Research Fund (P.S.) along with other funding bodies. P.S. is recipient of an honorary Professorship at University College London, UK. C.B. is a Ragnar Söderberg Fellow in Medicine and Cancerfonden Young Investigator. A.G. is an EMBO Postdoctoral Scholar and Barncancerfonded Postdoctoral Fellow. S.M. is a Cancerfonden Postdoctoral Fellow.

AUTHOR CONTRIBUTIONS

Conceptualization, C.B., M.M., and S.M.; methodology, M.M., S.M., A.K.-C., S.T., N.G., S.G., and C.B.; investigation, M.M., S.M., A.K.-C., H.F., S.T., A. G., A.C., K.K., C.A., Z.F., N.G., G.B., M.C., I.P.-G., A.H., A.C.-R., and C.B.; resources, C.D., P.S., H.K., H.-M.L., W.W.A., and D.B.; software, P.C.T.N.; formal analysis, P.C.T.N., M.M., S.M., V.S., C.A., K.K., S.G., A.K.-C., A. C.-R., and C.B.; data curation, P.C.T.N.; writing – original draft, C.B. and M. M.; writing – review & editing, C.B. and S.M.; supervision, C.B.; project administration, C.B.; funding acquisition, C.B.

DECLARATION OF INTERESTS

C.B. and S.M. are founders and members of the scientific advisory board of SACRA Therapeutics.

STAR★METHODS

Detailed methods are provided in the online version of this paper and include the following:

- KEY RESOURCES TABLE
- EXPERIMENTAL MODEL AND SUBJECT DETAILS
  - Patients and samples
  - Mouse strains
  - Cell culture
- METHOD DETAILS
  - Apoptosis analysis
  - Cell cycle analysis
  - siRNA-mediated gene knockdown
  - Transfection of synthetic tdRs
  - tdR quantification by SL-qPCR
  - Northern blot
  - RT-qPCR
  - Measurement of RIG-I-like receptors (RLRs) activity
  - Expression and purification of GFP-dRNase H1 D210N (GFP-dRH)
  - Imaging RNA-DNA hybrids with recombinant GFP-dRH
  - Western blotting
  - Global measurement of protein synthesis
  - Polysome fractionation
  - tdR-5-GlyGCC pulldowns
  - Liquid chromatography and mass spectrometry (LC-MS)
  - CUT&RUN
  - RNA-seq
  - Small RNA-seq
  - iCLIP-seq
  - RNA dot blot
  - Bleeding and isolation of bone marrow cells
  - Flow cytometric analysis
  - Poly I:C treatment
  - Transplantation
  - DSS colitis
  - Colonic lamina propria (cLP) cell isolation and flow cytometry
- QUANTIFICATION AND STATISTICAL ANALYSIS
  - RNA-seq data analysis
  - iCLIP-seq data analysis
  - Small RNA-seq analysis
  - Transposable element analysis
  - CUT&RUN analysis
  - Polysome-seq analysis
  - MS raw data processing and statistical analysis
  - PUS10 gene set signature analysis

SUPPLEMENTAL INFORMATION

Supplemental information can be found online at https://doi.org/10.1016/j.celrep.2025.115735.

Received: August 1, 2024
Revised: February 28, 2025
Accepted: May 2, 2025
Published: May 21, 2025

REFERENCES

1. Roundtree, I.A., Evans, M.E., Pan, T., and He, C. (2017). Dynamic RNA Modifications in Gene Expression Regulation. Cell *169*, 1187–1200. https://doi.org/10.1016/j.cell.2017.05.045.
2. Delaunay, S., and Frye, M. (2019). RNA modifications regulating cell fate in cancer. Nat. Cell Biol. *21*, 552–559. https://doi.org/10.1038/s41556-019-0319-0.
3. Charette, M., and Gray, M.W. (2000). Pseudouridine in RNA: what, where, how, and why. IUBMB Life *49*, 341–351. https://doi.org/10.1080/152165400410182.
4. Hamma, T., and Ferré-D'Amaré, A.R. (2006). Pseudouridine synthases. Chem. Biol. *13*, 1125–1135. https://doi.org/10.1016/j.chembiol.2006.09.009.
5. Ge, J., and Yu, Y.T. (2013). RNA pseudouridylation: new insights into an old modification. Trends Biochem. Sci. *38*, 210–218. https://doi.org/10.1016/j.tibs.2013.01.002.
6. Angrisani, A., Vicidomini, R., Turano, M., and Furia, M. (2014). Human dyskerin: beyond telomeres. Biol. Chem. *395*, 593–610. https://doi.org/10.1515/hsz-2013-0287.
7. Rintala-Dempsey, A.C., and Kothe, U. (2017). Eukaryotic stand-alone pseudouridine synthases - RNA modifying enzymes and emerging regulators of gene expression? RNA Biol. *14*, 1185–1196. https://doi.org/10.1080/15476286.2016.1276150.
8. Cerneckis, J., Cui, Q., He, C., Yi, C., and Shi, Y. (2022). Decoding pseudouridine: an emerging target for therapeutic development. Trends Pharmacol. Sci. *43*, 522–535. https://doi.org/10.1016/j.tips.2022.03.008.
9. Guzzi, N., Ciesla, M., Ngoc, P.C.T., Lang, S., Arora, S., Dimitriou, M., Pimkova, K., Sommarin, M.N.E., Munita, R., Lubas, M., et al. (2018). Pseudouridylation of tRNA-Derived Fragments Steers Translational Control in Stem Cells. Cell *173*, 1204–1216.e1226. https://doi.org/10.1016/j.cell.2018.03.008.
10. Guzzi, N., Muthukumar, S., Cieśla, M., Todisco, G., Ngoc, P.C.T., Madej, M., Munita, R., Fazio, S., Ekström, S., Mortera-Blanco, T., et al. (2022). Pseudouridine-modified tRNA fragments repress aberrant protein synthesis and predict leukaemic progression in myelodysplastic syndrome. Nat. Cell Biol. *24*, 299–306. https://doi.org/10.1038/s41556-022-00852-9.
11. Kfoury, Y.S., Ji, F., Mazzola, M., Sykes, D.B., Scherer, A.K., Anselmo, A., Akiyama, Y., Mercier, F., Severe, N., Kokkaliaris, K.D., et al. (2021). tiRNA signaling via stress-regulated vesicle transfer in the hematopoietic niche. Cell Stem Cell *28*, 2090–2103.e9. https://doi.org/10.1016/j.stem.2021.08.014.
12. Muthukumar, S., Li, C.T., Liu, R.J., and Bellodi, C. (2024). Roles and regulation of tRNA-derived small RNAs in animals. Nat. Rev. Mol. Cell Biol. *25*, 359–378. https://doi.org/10.1038/s41580-023-00690-z.
13. Goke, J., Lu, X., Chan, Y.S., Ng, H.H., Ly, L.H., Sachs, F., and Szczerbinska, I. (2015). Dynamic transcription of distinct classes of endogenous retroviral elements marks specific populations of early human embryonic cells. Cell Stem Cell *16*, 135–141. https://doi.org/10.1016/j.stem.2015.01.005.
14. Peaston, A.E., Evsikov, A.V., Graber, J.H., de Vries, W.N., Holbrook, A.E., Solter, D., and Knowles, B.B. (2004). Retrotransposons regulate host genes in mouse oocytes and preimplantation embryos. Dev. Cell *7*, 597–606. https://doi.org/10.1016/j.devcel.2004.09.004.
15. Svoboda, P., Stein, P., Anger, M., Bernstein, E., Hannon, G.J., and Schultz, R.M. (2004). RNAi and expression of retrotransposons MuERV-L and IAP in preimplantation mouse embryos. Dev. Biol. *269*, 276–285. https://doi.org/10.1016/j.ydbio.2004.01.028.
16. Gorbunova, V., Seluanov, A., Mita, P., McKerrow, W., Fenyö, D., Boeke, J.D., Linker, S.B., Gage, F.H., Kreiling, J.A., Petrashen, A.P., et al. (2021). The role of retrotransposable elements in ageing and age-associated diseases. Nature *596*, 43–53. https://doi.org/10.1038/s41586-021-03542-y.
17. Wang, J., Lu, X., Zhang, W., and Liu, G.H. (2024). Endogenous retroviruses in development and health. Trends Microbiol. *32*, 342–354. https://doi.org/10.1016/j.tim.2023.09.006.

18. Burns, K.H. (2020). Our Conflict with Transposable Elements and Its Implications for Human Disease. Annu. Rev. Pathol. *15*, 51–70. https://doi.org/10.1146/annurev-pathmechdis-012419-032633.

19. Jonsson, M.E., Garza, R., Johansson, P.A., and Jakobsson, J. (2020). Transposable Elements: A Common Feature of Neurodevelopmental and Neurodegenerative Disorders. Trends Genet. *36*, 610–623. https://doi.org/10.1016/j.tig.2020.05.004.

20. Kassiotis, G. (2023). The Immunological Conundrum of Endogenous Retroelements. Annu. Rev. Immunol. *41*, 99–125. https://doi.org/10.1146/annurev-immunol-101721-033341.

21. Wang, Y., Zhang, Z., He, H., Song, J., Cui, Y., Chen, Y., Zhuang, Y., Zhang, X., Li, M., Zhang, X., et al. (2023). Aging-induced pseudouridine synthase 10 impairs hematopoietic stem cells. Haematologica *108*, 2677–2689. https://doi.org/10.3324/haematol.2022.282211.

22. Jana, S., Hsieh, A.C., and Gupta, R. (2017). Reciprocal amplification of caspase-3 activity by nuclear export of a putative human RNA-modifying protein, PUS10 during TRAIL-induced apoptosis. Cell Death Dis. *8*, e3093. https://doi.org/10.1038/cddis.2017.476.

23. Song, J., Zhuang, Y., Zhu, C., Meng, H., Lu, B., Xie, B., Peng, J., Li, M., and Yi, C. (2020). Differential roles of human PUS10 in miRNA processing and tRNA pseudouridylation. Nat. Chem. Biol. *16*, 160–169. https://doi.org/10.1038/s41589-019-0420-5.

24. Festen, E.A.M., Goyette, P., Green, T., Boucher, G., Beauchamp, C., Trynka, G., Dubois, P.C., Lagacé, C., Stokkers, P.C.F., Hommes, D.W., et al. (2011). A meta-analysis of genome-wide association scans identifies IL18RAP, PTPN2, TAGAP, and PUS10 as shared risk loci for Crohn's disease and celiac disease. PLoS Genet. *7*, e1001283. https://doi.org/10.1371/journal.pgen.1001283.

25. Mankan, A.K., Schmidt, T., Chauhan, D., Goldeck, M., Höning, K., Gaidt, M., Kubarenko, A.V., Andreeva, L., Hopfner, K.P., and Hornung, V. (2014). Cytosolic RNA:DNA hybrids activate the cGAS-STING axis. EMBO J. *33*, 2937–2946. https://doi.org/10.15252/embj.201488726.

26. Medrano, L.M., Pascual, V., Bodas, A., López-Palacios, N., Salazar, I., Espino-Paisán, L., González-Pérez, B., Urcelay, E., Mendoza, J.L., and Núñez, C. (2019). Expression patterns common and unique to ulcerative colitis and celiac disease. Ann. Hum. Genet. *83*, 86–94. https://doi.org/10.1111/ahg.12293.

27. Deogharia, M., Mukhopadhyay, S., Joardar, A., and Gupta, R. (2019). The human ortholog of archaeal Pus10 produces pseudouridine 54 in select tRNAs where its recognition sequence contains a modified residue. RNA *25*, 336–351. https://doi.org/10.1261/rna.068114.118.

28. Joardar, A., Jana, S., Fitzek, E., Gurha, P., Majumder, M., Chatterjee, K., Geisler, M., and Gupta, R. (2013). Role of forefinger and thumb loops in production of Psi54 and Psi55 in tRNAs by archaeal Pus10. RNA *19*, 1279–1294. https://doi.org/10.1261/rna.039230.113.

29. Huppertz, I., Attig, J., D'Ambrogio, A., Easton, L.E., Sibley, C.R., Sugimoto, Y., Tajnik, M., König, J., and Ule, J. (2014). iCLIP: protein-RNA interactions at nucleotide resolution. Methods *65*, 274–287. https://doi.org/10.1016/j.ymeth.2013.10.011.

30. Loher, P., Telonis, A.G., and Rigoutsos, I. (2017). MINTmap: fast and exhaustive profiling of nuclear and mitochondrial tRNA fragments from short RNA-seq data. Sci. Rep. *7*, 41184. https://doi.org/10.1038/srep41184.

31. Thompson, D.M., Lu, C., Green, P.J., and Parker, R. (2008). tRNA cleavage is a conserved response to oxidative stress in eukaryotes. RNA *14*, 2095–2103. https://doi.org/10.1261/rna.1232808.

32. Yamasaki, S., Ivanov, P., Hu, G.F., and Anderson, P. (2009). Angiogenin cleaves tRNA and promotes stress-induced translational repression. J. Cell Biol. *185*, 35–42. https://doi.org/10.1083/jcb.200811106.

33. Blanco, S., Dietmann, S., Flores, J.V., Hussain, S., Kutter, C., Humphreys, P., Lukk, M., Lombard, P., Treps, L., Popis, M., et al. (2014). Aberrant methylation of tRNAs links cellular stress to neuro-developmental disorders. EMBO J. *33*, 2020–2039. https://doi.org/10.15252/embj.201489282.

34. Garcia-Vilchez, R., Anazco-Guenkova, A.M., Dietmann, S., Lopez, J., Moron-Calvente, V., D'Ambrosi, S., Nombela, P., Zamacola, K., Mendizabal, I., Garcia-Longarte, S., et al. (2023). METTL1 promotes tumorigenesis through tRNA-derived fragment biogenesis in prostate cancer. Mol. Cancer *22*, 119. https://doi.org/10.1186/s12943-023-01809-8.

35. Pezone, A., Olivieri, F., Napoli, M.V., Procopio, A., Avvedimento, E.V., and Gabrielli, A. (2023). Inflammation and DNA damage: cause, effect or both. Nat. Rev. Rheumatol. *19*, 200–211. https://doi.org/10.1038/s41584-022-00905-1.

36. Marchi, S., Guilbaud, E., Tait, S.W.G., Yamazaki, T., and Galluzzi, L. (2023). Mitochondrial control of inflammation. Nat. Rev. Immunol. *23*, 159–173. https://doi.org/10.1038/s41577-022-00760-x.

37. Sharma, U., Conine, C.C., Shea, J.M., Boskovic, A., Derr, A.G., Bing, X.Y., Belleannee, C., Kucukural, A., Serra, R.W., Sun, F., et al. (2016). Biogenesis and function of tRNA fragments during sperm maturation and fertilization in mammals. Science *351*, 391–396. https://doi.org/10.1126/science.aad6780.

38. Boskovic, A., Bing, X.Y., Kaymak, E., and Rando, O.J. (2020). Control of noncoding RNA production and histone levels by a 5' tRNA fragment. Genes Dev. *34*, 118–131. https://doi.org/10.1101/gad.332783.119.

39. Schorn, A.J., Gutbrod, M.J., LeBlanc, C., and Martienssen, R. (2017). LTR-Retrotransposon Control by tRNA-Derived Small RNAs. Cell *170*, 61–71.e11. https://doi.org/10.1016/j.cell.2017.06.013.

40. Jin, Y., Tam, O.H., Paniagua, E., and Hammell, M. (2015). TEtranscripts: a package for including transposable elements in differential expression analysis of RNA-seq datasets. Bioinformatics *31*, 3593–3599. https://doi.org/10.1093/bioinformatics/btv422.

41. Skene, P.J., Henikoff, J.G., and Henikoff, S. (2018). Targeted in situ genome-wide profiling with high efficiency for low cell numbers. Nat. Protoc. *13*, 1006–1019. https://doi.org/10.1038/nprot.2018.015.

42. de Regt, A.K., Anand, K., Ciupka, K., Bender, F., Gatterdam, K., Putschli, B., Fusshöller, D., Hilbig, D., Kirchhoff, A., Hunkler, C., et al. (2023). A conserved isoleucine in the binding pocket of RIG-I controls immune tolerance to mitochondrial RNA. Nucleic Acids Res. *51*, 11893–11910. https://doi.org/10.1093/nar/gkad835.

43. Rehwinkel, J., and Gack, M.U. (2020). RIG-I-like receptors: their regulation and roles in RNA sensing. Nat. Rev. Immunol. *20*, 537–551. https://doi.org/10.1038/s41577-020-0288-3.

44. Crossley, M.P., Brickner, J.R., Song, C., Zar, S.M.T., Maw, S.S., Chédin, F., Tsai, M.S., and Cimprich, K.A. (2021). Catalytically inactive, purified RNase H1: A specific and sensitive probe for RNA-DNA hybrid imaging. J. Cell Biol. *220*, e202101092. https://doi.org/10.1083/jcb.202101092.

45. Zhao, Y., Oreskovic, E., Zhang, Q., Lu, Q., Gilman, A., Lin, Y.S., He, J., Zheng, Z., Lu, J.Y., Lee, J., et al. (2021). Transposon-triggered innate immune response confers cancer resistance to the blind mole rat. Nat. Immunol. *22*, 1219–1230. https://doi.org/10.1038/s41590-021-01027-8.

46. Haag, S.M., Gulen, M.F., Reymond, L., Gibelin, A., Abrami, L., Decout, A., Heymann, M., van der Goot, F.G., Turcatti, G., Behrendt, R., and Ablasser, A. (2018). Targeting STING with covalent small-molecule inhibitors. Nature *559*, 269–273. https://doi.org/10.1038/s41586-018-0287-8.

47. Gluck, S., Guey, B., Gulen, M.F., Wolter, K., Kang, T.W., Schmacke, N.A., Bridgeman, A., Rehwinkel, J., Zender, L., and Ablasser, A. (2017). Innate immune sensing of cytosolic chromatin fragments through cGAS promotes senescence. Nat. Cell Biol. *19*, 1061–1070. https://doi.org/10.1038/ncb3586.

48. Zhang, Z., Kim, T., Bao, M., Facchinetti, V., Jung, S.Y., Ghaffari, A.A., Qin, J., Cheng, G., and Liu, Y.J. (2011). DDX1, DDX21, and DHX36 helicases form a complex with the adaptor molecule TRIF to sense dsRNA in dendritic cells. Immunity *34*, 866–878. https://doi.org/10.1016/j.immuni.2011.03.027.

49. Islam, Z., Polash, A., Suzawa, M., Chim, B., Kuhn, S., Sultana, S., Cutrona, N., Smith, P.T., Kabat, J., Ganesan, S., et al. (2024). MATRIN3 deficiency triggers autoinflammation via cGAS-STING activation. Preprint at bioRxiv. https://doi.org/10.1101/2024.04.01.587645.

50. Peng, Y., Guo, J., Sun, T., Fu, Y., Zheng, H., Dong, C., and Xiong, S. (2020). USP39 Serves as a Deubiquitinase to Stabilize STAT1 and Sustains Type I IFN-Induced Antiviral Immunity. J. Immunol. *205*, 3167–3178. https://doi.org/10.4049/jimmunol.1901384.

51. Quan, J., Zhao, X., Xiao, Y., Wu, H., Di, Q., Wu, Z., Chen, X., Tang, H., Zhao, J., Guan, Y., et al. (2023). USP39 Regulates NF-kappaB-Mediated Inflammatory Responses through Deubiquitinating K48-Linked IkappaBalpha. J. Immunol. *210*, 640–652. https://doi.org/10.4049/jimmunol.2200603.

52. Takizawa, H., Boettcher, S., and Manz, M.G. (2012). Demand-adapted regulation of early hematopoiesis in infection and inflammation. Blood *119*, 2991–3002. https://doi.org/10.1182/blood-2011-12-380113.

53. Caiado, F., Pietras, E.M., and Manz, M.G. (2021). Inflammation as a regulator of hematopoietic stem cell function in disease, aging, and clonal selection. J. Exp. Med. *218*, e20201541. https://doi.org/10.1084/jem.20201541.

54. Lemerle, E., and Trompouki, E. (2023). Transposable elements in normal and malignant hematopoiesis. Dis. Model. Mech. *16*, dmm050170. https://doi.org/10.1242/dmm.050170.

55. Clapes, T., Polyzou, A., Prater, P., Hummel, B., Morales-Hernandez, A., Morales-Hernández, A., Ferrarini, M.G., Kehrer, N., Lefkopoulos, S., Bergo, V., et al. (2021). Chemotherapy-induced transposable elements activate MDA5 to enhance haematopoietic regeneration. Nat. Cell Biol. *23*, 704–717. https://doi.org/10.1038/s41556-021-00707-9.

56. Gerber, J.P., Russ, J., Chandrasekar, V., Offermann, N., Lee, H.M., Spear, S., Guzzi, N., Maida, S., Pattabiraman, S., Zhang, R., et al. (2021). Aberrant chromatin landscape following loss of the H3.3 chaperone Daxx in haematopoietic precursors leads to Pu.1-mediated neutrophilia and inflammation. Nat. Cell Biol. *23*, 1224–1239. https://doi.org/10.1038/s41556-021-00774-y.

57. Ishida, T., Suzuki, S., Lai, C.Y., Yamazaki, S., Kakuta, S., Iwakura, Y., Nojima, M., Takeuchi, Y., Higashihara, M., Nakauchi, H., and Otsu, M. (2017). Pre-Transplantation Blockade of TNF-alpha-Mediated Oxygen Species Accumulation Protects Hematopoietic Stem Cells. Stem Cell. *35*, 989–1002. https://doi.org/10.1002/stem.2524.

58. Hill, G.R. (2009). Inflammation and bone marrow transplantation. Biol. Blood Marrow Transplant. *15*, 139–141. https://doi.org/10.1016/j.bbmt.2008.11.008.

59. Pietras, E.M., Lakshminarasimhan, R., Techner, J.M., Fong, S., Flach, J., Binnewies, M., and Passegué, E. (2014). Re-entry into quiescence protects hematopoietic stem cells from the killing effect of chronic exposure to type I interferons. J. Exp. Med. *211*, 245–262. https://doi.org/10.1084/jem.20131043.

60. Crow, Y.J., and Stetson, D.B. (2022). The type I interferonopathies: 10 years on. Nat. Rev. Immunol. *22*, 471–483. https://doi.org/10.1038/s41577-021-00633-9.

61. Kaul, A., Gordon, C., Crow, M.K., Touma, Z., Urowitz, M.B., van Vollenhoven, R., Ruiz-Irastorza, G., and Hughes, G. (2016). Systemic lupus erythematosus. Nat. Rev. Dis. Primers *2*, 16039. https://doi.org/10.1038/nrdp.2016.39.

62. Sandling, J.K., Pucholt, P., Hultin Rosenberg, L., Farias, F.H.G., Kozyrev, S.V., Eloranta, M.L., Alexsson, A., Bianchi, M., Padyukov, L., Bengtsson, C., et al. (2021). Molecular pathways in patients with systemic lupus erythematosus revealed by gene-centred DNA sequencing. Ann. Rheum. Dis. *80*, 109–117. https://doi.org/10.1136/annrheumdis-2020-218636.

63. Hutcheson, J., Scatizzi, J.C., Siddiqui, A.M., Haines, G.K., 3rd, Wu, T., Li, Q.Z., Davis, L.S., Mohan, C., and Perlman, H. (2008). Combined deficiency of proapoptotic regulators Bim and Fas results in the early onset of systemic autoimmunity. Immunity *28*, 206–217. https://doi.org/10.1016/j.immuni.2007.12.015.

64. Vanhove, W., Peeters, P.M., Staelens, D., Schraenen, A., Van der Goten, J., Cleynen, I., De Schepper, S., Van Lommel, L., Reynaert, N.L., Schuit, F., et al. (2015). Strong Upregulation of AIM2 and IFI16 Inflammasomes in the Mucosa of Patients with Active Inflammatory Bowel Disease. Inflamm. Bowel Dis. *21*, 2673–2682. https://doi.org/10.1097/MIB.0000000000000535.

65. Sole, X., Crous-Bou, M., Cordero, D., Olivares, D., Guino, E., Sanz-Pamplona, R., Rodriguez-Moranta, F., Sanjuan, X., de Oca, J., Salazar, R., and Moreno, V. (2014). Discovery and validation of new potential biomarkers for early detection of colon cancer. PLoS One *9*, e106748. https://doi.org/10.1371/journal.pone.0106748.

66. Luda, K.M., Joeris, T., Persson, E.K., Rivollier, A., Demiri, M., Sitnik, K.M., Pool, L., Holm, J.B., Melo-Gonzalez, F., Richter, L., et al. (2016). IRF8 Transcription-Factor-Dependent Classical Dendritic Cells Are Essential for Intestinal T Cell Homeostasis. Immunity *44*, 860–874. https://doi.org/10.1016/j.immuni.2016.02.008.

67. Cui, L., Ma, R., Cai, J., Guo, C., Chen, Z., Yao, L., Wang, Y., Fan, R., Wang, X., and Shi, Y. (2022). RNA modifications: importance in immune cell biology and related diseases. Signal Transduct. Target. Ther. *7*, 334. https://doi.org/10.1038/s41392-022-01175-9.

68. Kuhle, B., Chen, Q., and Schimmel, P. (2023). tRNA renovatio: Rebirth through fragmentation. Mol. Cell *83*, 3953–3971. https://doi.org/10.1016/j.molcel.2023.09.016.

69. Kim, J.J., Lee, S.Y., Hwang, Y., Kim, S., Chung, J.M., Park, S., Yoon, J., Yun, H., Ji, J.H., Chae, S., et al. (2021). USP39 promotes non-homologous end-joining repair by poly(ADP-ribose)-induced liquid demixing. Nucleic Acids Res. *49*, 11083–11102. https://doi.org/10.1093/nar/gkab892.

70. Hou, Y., Li, Y., Xiang, J.F., Tilahun, K., Jiang, J., Corces, V.G., and Yao, B. (2024). TDP-43 chronic deficiency leads to dysregulation of transposable elements and gene expression by affecting R-loop and 5hmC crosstalk. Cell Rep. *43*, 113662. https://doi.org/10.1016/j.celrep.2023.113662.

71. Yang, X., Li, G., Lou, P., Zhang, M., Yao, K., Xiao, J., Chen, Y., Xu, J., Tian, S., Deng, M., et al. (2024). Excessive nucleic acid R-loops induce mitochondria-dependent epithelial cell necroptosis and drive spontaneous intestinal inflammation. Proc. Natl. Acad. Sci. USA *121*, e2307395120. https://doi.org/10.1073/pnas.2307395120.

72. Goodier, J.L., Cheung, L.E., and Kazazian, H.H., Jr. (2012). MOV10 RNA helicase is a potent inhibitor of retrotransposition in cells. PLoS Genet. *8*, e1002941. https://doi.org/10.1371/journal.pgen.1002941.

73. Lu, C., Luo, Z., Jäger, S., Krogan, N.J., and Peterlin, B.M. (2012). Moloney leukemia virus type 10 inhibits reverse transcription and retrotransposition of intracisternal a particles. J. Virol. *86*, 10517–10523. https://doi.org/10.1128/JVI.00868-12.

74. Gregersen, L.H., Schueler, M., Munschauer, M., Mastrobuoni, G., Chen, W., Kempa, S., Dieterich, C., and Landthaler, M. (2014). MOV10 Is a 5' to 3' RNA helicase contributing to UPF1 mRNA target degradation by translocation along 3' UTRs. Mol. Cell *54*, 573–585. https://doi.org/10.1016/j.molcel.2014.03.017.

75. Liu, W., Wang, Z., Liu, L., Yang, Z., Liu, S., Ma, Z., Liu, Y., Ma, Y., Zhang, L., Zhang, X., et al. (2020). LncRNA Malat1 inhibition of TDP43 cleavage suppresses IRF3-initiated antiviral innate immunity. Proc. Natl. Acad. Sci. USA *117*, 23695–23706. https://doi.org/10.1073/pnas.2003932117.

76. Cuevas, R.A., Ghosh, A., Wallerath, C., Hornung, V., Coyne, C.B., and Sarkar, S.N. (2016). MOV10 Provides Antiviral Activity against RNA Viruses by Enhancing RIG-I-MAVS-Independent IFN Induction. J. Immunol. *196*, 3877–3886. https://doi.org/10.4049/jimmunol.1501359.

77. Schorn, A.J., and Martienssen, R. (2018). Tie-Break: Host and Retrotransposons Play tRNA. Trends Cell Biol. *28*, 793–806. https://doi.org/10.1016/j.tcb.2018.05.006.

78. Chen, L., Xu, W., Liu, K., Jiang, Z., Han, Y., Jin, H., Zhang, L., Shen, W., Jia, S., Sun, Q., and Meng, A. (2021). 5' Half of specific tRNAs feeds back to promote corresponding tRNA gene transcription in vertebrate embryos. Sci. Adv. *7*, eabh0494. https://doi.org/10.1126/sciadv.abh0494.

79. Crossley, M.P., Song, C., Bocek, M.J., Choi, J.H., Kousouros, J.N., Sathirachinda, A., Lin, C., Brickner, J.R., Bai, G., Lans, H., et al. (2023). R-loop-derived cytoplasmic RNA-DNA hybrids activate an immune response. Nature *613*, 187–194. https://doi.org/10.1038/s41586-022-05545-9.

80. Tosar, J.P., Gámbaro, F., Darré, L., Pantano, S., Westhof, E., and Cayota, A. (2018). Dimerization confers increased stability to nucleases in 5' halves from glycine and glutamic acid tRNAs. Nucleic Acids Res. *46*, 9081–9093. https://doi.org/10.1093/nar/gky495.

81. Costa, B., Li Calzi, M., Castellano, M., Blanco, V., Cuevasanta, E., Litvan, I., Ivanov, P., Witwer, K., Cayota, A., and Tosar, J.P. (2023). Nicked tRNAs are stable reservoirs of tRNA halves in cells and biofluids. Proc. Natl. Acad. Sci. USA *120*, e2216330120. https://doi.org/10.1073/pnas.2216330120.

82. Lyons, S.M., Gudanis, D., Coyne, S.M., Gdaniec, Z., and Ivanov, P. (2017). Identification of functional tetramolecular RNA G-quadruplexes derived from transfer RNAs. Nat. Commun. *8*, 1127. https://doi.org/10.1038/s41467-017-01278-w.

83. Chen, X., and Wolin, S.L. (2023). Transfer RNA halves are found as nicked tRNAs in cells: evidence that nicked tRNAs regulate expression of an RNA repair operon. RNA *29*, 620–629. https://doi.org/10.1261/rna.079575.122.

84. Zhang, Y., Zhang, X., Shi, J., Tuorto, F., Li, X., Liu, Y., Liebers, R., Zhang, L., Qu, Y., Qian, J., et al. (2018). Dnmt2 mediates intergenerational transmission of paternally acquired metabolic disorders through sperm small non-coding RNAs. Nat. Cell Biol. *20*, 535–540. https://doi.org/10.1038/s41556-018-0087-2.

85. Chen, Z., Qi, M., Shen, B., Luo, G., Wu, Y., Li, J., Lu, Z., Zheng, Z., Dai, Q., and Wang, H. (2019). Transfer RNA demethylase ALKBH3 promotes cancer progression via induction of tRNA-derived small RNAs. Nucleic Acids Res. *47*, 2533–2545. https://doi.org/10.1093/nar/gky1250.

86. Saferding, V., and Blüml, S. (2020). Innate immunity as the trigger of systemic autoimmune diseases. J. Autoimmun. *110*, 102382. https://doi.org/10.1016/j.jaut.2019.102382.

87. Kamada, R., Yang, W., Zhang, Y., Patel, M.C., Yang, Y., Ouda, R., Dey, A., Wakabayashi, Y., Sakaguchi, K., Fujita, T., et al. (2018). Interferon stimulation creates chromatin marks and establishes transcriptional memory. Proc. Natl. Acad. Sci. USA *115*, E9162–E9171. https://doi.org/10.1073/pnas.1720930115.

88. Chuong, E.B., Elde, N.C., and Feschotte, C. (2016). Regulatory evolution of innate immunity through co-option of endogenous retroviruses. Science *351*, 1083–1087. https://doi.org/10.1126/science.aad5497.

89. Kazachenka, A., Young, G.R., Attig, J., Kordella, C., Lamprianidou, E., Zoulia, E., Vrachiolias, G., Papoutselis, M., Bernard, E., Papaemmanuil, E., et al. (2019). Epigenetic therapy of myelodysplastic syndromes connects to cellular differentiation independently of endogenous retroelement derepression. Genome Med. *11*, 86. https://doi.org/10.1186/s13073-019-0707-x.

90. Schumann, G.G., Fuchs, N.V., Tristán-Ramos, P., Sebe, A., Ivics, Z., and Heras, S.R. (2019). The impact of transposable element activity on therapeutically relevant human stem cells. Mobile DNA *10*, 9. https://doi.org/10.1186/s13100-019-0151-x.

91. Zhang, M., Wang, Y., Wang, Y., Bai, Y., and Gu, D. (2022). Association Between Systemic Lupus Erythematosus and Cancer Morbidity and Mortality: Findings From Cohort Studies. Front. Oncol. *12*, 860794. https://doi.org/10.3389/fonc.2022.860794.

92. Axelrad, J.E., Lichtiger, S., and Yajnik, V. (2016). Inflammatory bowel disease and cancer: The role of inflammation, immunosuppression, and cancer treatment. World J. Gastroenterol. *22*, 4794–4801. https://doi.org/10.3748/wjg.v22.i20.4794.

93. Kanke, M., Kennedy Ng, M.M., Connelly, S., Singh, M., Schaner, M., Shanahan, M.T., Wolber, E.A., Beasley, C., Lian, G., Jain, A., et al. (2022). Single-Cell Analysis Reveals Unexpected Cellular Changes and Transposon Expression Signatures in the Colonic Epithelium of Treatment-Naive Adult Crohn's Disease Patients. Cell. Mol. Gastroenterol. Hepatol. *13*, 1717–1740. https://doi.org/10.1016/j.jcmgh.2022.02.005.

94. Lima-Junior, D.S., Krishnamurthy, S.R., Bouladoux, N., Collins, N., Han, S.J., Chen, E.Y., Constantinides, M.G., Link, V.M., Lim, A.I., Enamorado, M., et al. (2021). Endogenous retroviruses promote homeostatic and inflammatory responses to the microbiota. Cell *184*, 3794–3811.e19. https://doi.org/10.1016/j.cell.2021.05.020.

95. Langmead, B., Trapnell, C., Pop, M., and Salzberg, S.L. (2009). Ultrafast and memory-efficient alignment of short DNA sequences to the human genome. Genome Biol. *10*, R25. https://doi.org/10.1186/gb-2009-10-3-r25.

96. Uren, P.J., Bahrami-Samani, E., Burns, S.C., Qiao, M., Karginov, F.V., Hodges, E., Hannon, G.J., Sanford, J.R., Penalva, L.O.F., and Smith, A.D. (2012). Site identification in high-throughput RNA-protein interaction data. Bioinformatics *28*, 3013–3020. https://doi.org/10.1093/bioinformatics/bts569.

97. Bailey, T.L., Johnson, J., Grant, C.E., and Noble, W.S. (2015). The MEME Suite. Nucleic Acids Res. *43*, W39–W49. https://doi.org/10.1093/nar/gkv416.

98. Chan, P.P., and Lowe, T.M. (2016). GtRNAdb 2.0: an expanded database of transfer RNA genes identified in complete and draft genomes. Nucleic Acids Res. *44*, D184–D189. https://doi.org/10.1093/nar/gkv1309.

99. Hao, Y., Hao, S., Andersen-Nissen, E., Mauck, W.M., 3rd, Zheng, S., Butler, A., Lee, M.J., Wilk, A.J., Darby, C., Zager, M., et al. (2021). Integrated analysis of multimodal single-cell data. Cell *184*, 3573–3587.e29. https://doi.org/10.1016/j.cell.2021.04.048.

100. Wolf, F.A., Angerer, P., and Theis, F.J. (2018). SCANPY: large-scale single-cell gene expression data analysis. Genome Biol. *19*, 15. https://doi.org/10.1186/s13059-017-1382-0.

101. Dobin, A., Davis, C.A., Schlesinger, F., Drenkow, J., Zaleski, C., Jha, S., Batut, P., Chaisson, M., and Gingeras, T.R. (2013). STAR: ultrafast universal RNA-seq aligner. Bioinformatics *29*, 15–21. https://doi.org/10.1093/bioinformatics/bts635.

102. Love, M.I., Huber, W., and Anders, S. (2014). Moderated estimation of fold change and dispersion for RNA-seq data with DESeq2. Genome Biol. *15*, 550. https://doi.org/10.1186/s13059-014-0550-8.

103. Foroutan, M., Bhuva, D.D., Lyu, R., Horan, K., Cursons, J., and Davis, M.J. (2018). Single sample scoring of molecular phenotypes. BMC Bioinf. *19*, 404. https://doi.org/10.1186/s12859-018-2435-4.

104. Subramanian, A., Tamayo, P., Mootha, V.K., Mukherjee, S., Ebert, B.L., Gillette, M.A., Paulovich, A., Pomeroy, S.L., Golub, T.R., Lander, E.S., and Mesirov, J.P. (2005). Gene set enrichment analysis: a knowledge-based approach for interpreting genome-wide expression profiles. Proc. Natl. Acad. Sci. USA *102*, 15545–15550. https://doi.org/10.1073/pnas.0506580102.

105. Huang, T., Choi, M., Tzouros, M., Golling, S., Pandya, N.J., Banfai, B., Dunkley, T., and Vitek, O. (2020). MSstatsTMT: Statistical Detection of Differentially Abundant Proteins in Experiments with Isobaric Labeling and Multiple Mixtures. Mol. Cell. Proteomics *19*, 1706–1723. https://doi.org/10.1074/mcp.RA120.002105.

106. Smyth, G.K. (2004). Linear models and empirical bayes methods for assessing differential expression in microarray experiments. Stat. Appl. Genet. Mol. Biol. *3*, Article3. https://doi.org/10.2202/1544-6115.1027.

107. Ciesla, M., Ngoc, P.C.T., Cordero, E., Martinez, A.S., Morsing, M., Muthukumar, S., Beneventi, G., Madej, M., Munita, R., Jonsson, T., et al. (2021). Oncogenic translation directs spliceosome dynamics revealing an integral role for SF3A3 in breast cancer. Mol. Cell *81*, 1453–1468.e1412. https://doi.org/10.1016/j.molcel.2021.01.034.

108. Smith, T., Heger, A., and Sudbery, I. (2017). UMI-tools: modeling sequencing errors in Unique Molecular Identifiers to improve quantification accuracy. Genome Res. *27*, 491–499. https://doi.org/10.1101/gr.209601.116.

109. Melmed, S. (2009). Acromegaly pathogenesis and treatment. J. Clin. Investig. *119*, 3189–3202, 39375 [pii]. https://doi.org/10.1172/JCI39375.

110. Liberzon, A., Birger, C., Thorvaldsdóttir, H., Ghandi, M., Mesirov, J.P., and Tamayo, P. (2015). The Molecular Signatures Database (MSigDB) hallmark gene set collection. Cell Syst. *1*, 417–425. https://doi.org/10.1016/j.cels.2015.12.004.

111. Perez, R.K., Gordon, M.G., Subramaniam, M., Kim, M.C., Hartoularos, G. C., Targ, S., Sun, Y., Ogorodnikov, A., Bueno, R., Lu, A., et al. (2022). Single-cell RNA-seq reveals cell type-specific molecular and genetic associations to lupus. Science *376*, eabf1970. https://doi.org/10.1126/science.abf1970.

112. Parikh, K., Antanaviciute, A., Fawkner-Corbett, D., Jagielowicz, M., Aulicino, A., Lagerholm, C., Davis, S., Kinchen, J., Chen, H.H., Alham, N.K., et al. (2019). Colonic epithelial cell diversity in health and inflammatory bowel disease. Nature *567*, 49–55. https://doi.org/10.1038/s41586-019-0992-y.

STAR★METHODS

KEY RESOURCES TABLE

REAGENT or RESOURCE	SOURCE	IDENTIFIER
Antibodies		
Anti-Pus10 rabbit polyclonal antibody	This paper	N/A
Anti-Vinculin	Sigma	CAT# V4505; RRID:AB_477617
Anti-cGAS (D3O8O)	Cell Signaling	CAT#31659; RRID:AB_2799008
Anti-STING (D2P2F)	Cell Signaling	CAT#13647; RRID:AB_2732796
Anti-pSTING (D7C3S)	Cell Signaling	CAT#19781; RRID:AB_2737062
Anti-IRF3 (D83B9)	Cell Signaling	CAT#4302; RRID:AB_1904036
Anti-pIRF3 (4D4G)	Cell Signaling	CAT#4947; RRID:AB_823547
Anti-DNA-RNA Hybrid [S9.6]	Kerafast	CAT#ENH002; RRID:AB_2687463
Anti-dsRNA [J2]	Jena Bioscience	CAT#RNT-SCI-10010200; RRID:AB_2922431
Anti-USP39 (E8U2M)	Cell Signaling	CAT#23303
Anti-Tardbp	Abcam	CAT#ab109535; RRID:AB_10859634
Anti-DHX36	Proteintech	CAT#13159-1-AP; RRID:AB_2092157
Anti-Mov10	Invitrogen	CAT#MA5-57488
APC/Cyanine7 anti-mouse/human CD45R/B220 Antibody (clone RA3-6B2)	BioLegend	CAT#103224; RRID:AB_313007
CD45 Monoclonal Antibody (Clone 30-F11), FITC	BioLegend	CAT#11-0451-82; RRID:AB_465050
Ly-6G Monoclonal Antibody (Clone 1A8-Ly6g), PE	eBioscience	CAT#12-9668-82; RRID:AB_2572720
TCR beta Monoclonal Antibody (H57-597), APC	eBioscience	CAT#17-5961-82; RRID:AB_469481
PE anti-mouse Ly-6G/Ly-6C (Gr-1) Antibody (clone RB6-8C5)	BioLegend	CAT#108407; RRID:AB_313372
PE anti-mouse/human CD11b Antibody (clone M1/70)	BioLegend	CAT#101208; RRID:AB_312791
Pacific Blue™ anti-mouse CD3 Antibody (clone 17A2)	BioLegend	CAT#100214; RRID:AB_493645
PE/Cyanine5 anti-mouse TER-119/Erythroid Cells Antibody (clone TER-119)	BioLegend	CAT#116210; RRID:AB_313711
PE/Cyanine5 anti-mouse Ly-6G/Ly-6C (Gr-1) Antibody (clone RB6-8C5)	BioLegend	CAT#108410; RRID:AB_313375
PE/Cyanine5 anti-mouse/human CD45R/B220 Antibody (clone RA3-6B2)	BioLegend	CAT#103210; RRID:AB_312495
PE/Cyanine5 anti-mouse CD3e Antibody (clone 145-2C11)	BioLegend	CAT#100310; RRID:AB_312675
APC anti-mouse CD117 (c-Kit) Antibody (clone 2B8)	BioLegend	CAT#105812; RRID:AB_313221
PE/Cyanine7 anti-mouse Ly-6A/E (Sca-1) Antibody (clone D7)	BioLegend	CAT#108114; RRID:AB_493596
APC/Cyanine7 anti-mouse CD48 Antibody (clone HM48-1)	BioLegend	CAT#103432; RRID:AB_2561463
Brilliant Violet 605™ anti-mouse CD150 (SLAM) Antibody (clone TC15-12F12.2)	BioLegend	CAT#115927; RRID:AB_11204248
PE/Cyanine7 anti-mouse CD19 Antibody (clone 6D5)	SONY	CAT#1177600
CD19 Monoclonal Antibody (clone1D3)	eBioscience	CAT#17886921
Alexa Fluor 700 anti-mouse CD3 Antibody (clone 17A2)	SONY	CAT#1101080; AB_2935667
APC anti-mouse/human CD11b Antibody (clone M1/70)	SONY	CAT#1106060
Pacific Blue™ anti-mouse NK-1.1 Antibody (clone PK136)	SONY	CAT#1143610

(*Continued on next page*)

Continued

REAGENT or RESOURCE	SOURCE	IDENTIFIER
Brilliant Violet 650™ anti-mouse CD45.1 Antibody (clone A20)	SONY	CAT#1153680
Brilliant Violet 785™ anti-mouse CD45.2 Antibody (clone 104)	SONY	CAT#1149195
PE/Cyanine5 anti-mouse NK-1.1 Antibody (clone PK136)	BioLegend	CAT#108716; RRID:AB_493590
APC-eFluor™ 780 anti-mouse CD117 (c-Kit) Antibody (clone 2B8), eBioscience™	Invitrogen	CAT#47-1171-82; RRID:AB_1272177
Pacific Blue™ anti-mouse Ly-6A/E (Sca-1) Antibody (clone E13–161.7)	BioLegend	CAT#122520; RRID:AB_2143237
FITC anti-mouse CD48 Antibody (clone HM48-1)	BioLegend	CAT#103404; RRID:AB_313019
PE/Cyanine7 anti-mouse CD150 (SLAM) Antibody (clone TC15-12F12.2)	BioLegend	CAT#115914; RRID:AB_439797
APC anti-mouse CD201 (EPCR) Antibody (clone eBio1560), eBioscience™	Invitrogen	CAT#17-2012-82; RRID: AB_10717805
PE Anti-mouse CD135 Antibody (clone A2F10)	SONY	CAT#1276530
Biotin anti-mouse CD127 Antibody (clone A7R34)	SONY	CAT#1275030
Qdot™ 605 Streptavidin Conjugate	Invitrogen	CAT#Q10101MP
Purified anti-mouse CD16/32 (Mouse BD Fc block™, clone 2.4G2)	BD Pharmingen	CAT# 553142; RRID: AB_394657
Annexin V, FITC conjugate	Thermo Fisher Scientific	CAT# A35111
Annexin V, PE conjugate	Thermo Fisher Scientific	CAT# A13199
Goat Anti-Rabbit IgG H&L	Abcam	CAT#97047
Histone H3K4me3 antibody	Active Motif	CAT#39519
BD Pharmingen™ FITC BrdU Flow Kit	BD Biosciences	CAT#AB_2617060; RRID:AB_2617060
Dynabeads Protein A	Thermo Fisher Scientific	CAT#10442945
Bacterial and Virus Strains		
One Shot Stbl3 Chemically Competent E. coli	Thermo Fisher Scientific	CAT#C737303
One Shot™ TOP10 Chemically Competent E. coli	Thermo Fisher Scientific	CAT# C404010
BL21(DE3) Competent Cells	Thermo Fisher Scientific	EC0114
Chemicals, Peptides, and Recombinant Proteins		
cOmplete™, Mini, EDTA-free Protease Inhibitor Cocktail	Sigma-Aldrich	CAT#04693159001 ROCHE
PhosSTOP™	Sigma-Aldrich	CAT#PHOSS-RO ROCHE
RNase A	Sigma-Aldrich	CAT#R4875
RNase I	ThermoFisher	CAT#AM2294
RNase III	Invitrogen	AM2290
RNase H	NEB	M0297
TURBO DNA-free™ Kit	ThermoFisher	CAT# AM2238
T4 PNK	NEB	CAT# M0201
SUPERase-IN RNase Inhibitor	ThermoFisher	CAT# AM2694
T4 RNA Ligase I	NEB	CAT# M0204
PEG400	Sigma-Aldrich	CAT# 202398
ATP, [γ-32P]- 3000 Ci/mmol 10 mCi/ml EasyTide Lead	Perkin Elmer	CAT# NEG502A250UC
EasyTag EXPRESS^{35} S Protein Labeling Mix, [^{35}S]-, 2mCi	Perkin Elmer	NEG772002MC
PerfectHyb Plus hybridization buffer	Sigma-Aldrich	CAT# H7033
Amersham Hybond-N+ membrane	GE Healthcare	CAT# RPN203
Herring Sperm DNA	ThermoFisher	CAT# 15634017
NuPAGE LDS Sample Buffer (4X)	ThermoFisher	CAT# NP007
NuPAGE™ 4–12% Bis-Tris Protein Gels	ThermoFisher	CAT# NP0321BOX
Amersham Protran 0.45 NC	GE Healthcare	CAT# 10600002
Doxycycline hyclate	Sigma-Aldrich	CAT# D9891

(*Continued on next page*)

Continued

REAGENT or RESOURCE	SOURCE	IDENTIFIER
TRIzol™ Reagent	Thermo Fisher Scientific	CAT#15596026
RNA 6000 Nano Bioanalyzer kit	Agilent Technologies	CAT# 5067-1511
High Sensitivity DNA Bioanalyzer kit	Agilent Technologies	CAT# 5067-4626
Polybrene	Santa Cruz Biotechnology	CAT# sc-134220
RNaseOUT™ Recombinant Ribonuclease Inhibitor	Thermo Fisher Scientific	CAT#10777019
SsoAdvanced™ Universal SYBR® Green Supermix	BioRad	CAT#1725274
TaKaRa Taq™ DNA Polymerase	TaKaRa	CAT#R0001A
4–20% Mini-PROTEAN® TGX™ Precast Protein Gels	BioRad	CAT#4561093
Propidium Iodide	Sigma-Aldrich	CAT#P4170
DAPI (4′,6-diamidino-2-Phenylindole, dihydrochloride)	Thermo Fisher Scientific	CAT# D1306
Lamivudine (3TC)	Sigma-Aldrich	CAT# L1295
BD Horizon™ Brilliant Stain Buffer	BD Biosciences	CAT#563794
DMEM HG	Thermo Fisher Scientific	11594496
Gelatin	Sigma-Aldrich	G1393
b-mercaptoethanol	Gibco	CAT#31350010
MTT	Sigma	M-5655
H-151	Sigma	SML2437
Dextran sulfate sodium (DSS)	Merck	265152
Poly (I:C) HMW	InvivoGen	CAT#tlrl-pic-5
Ciprofloxacin	HEXAL	N/A
ON-TARGETplus non-targeting siRNA	Dharmacon	CAT#D-001810-01-0005
ON-TARGETplus Mouse cGAS SMART pool siRNA	Dharmacon	Cat #L-055608
ON-TARGETplus Human PUS10 SMART pool	Dharmacon	Cat #L015635
ON-TARGETplus Mouse Mavs SMART pool siRNA	Dharmacon	Cat #L-053767
Critical Commercial Assays		
TruSeq Stranded Total RNA Library Prep Gold (48 Samples)	Illumina	CAT#20020598
NEXTFLEX® Small RNA-Seq Kit v4	PerkinElmer, Inc.	CAT#NOVA-5132-06
NextSeq 500/550 High Output v2.5 kit (75 cycles)	Illumina	CAT# 20024906
KAPA HyperPrep Kit	Roche	07962347001
Direct-zol™ RNA Miniprep	Zymo Research	CAT# R2052
Direct-zol™ RNA MicroPrep Plus	Zymo Research	CAT# R2062
RNA Clean & Concentrator™-5	Zymo Research	CAT# R1014
Quick Start™ Bradford Protein Assay Kit	BioRad	CAT#5000201
PEG Virus Precipitation Kit	BioVision	CAT# K904-50
High-Capacity cDNA Reverse Transcription Kit	Thermo Fisher Scientific	CAT#4368814
Deposited Data		
Raw and analyzed data: RNA-seq	This paper	GEO: GSE248959
Raw and analyzed data: smRNA-seq	This paper	GEO: GSE248959
Raw and analyzed data: iCLIP-seq	This paper	GEO: GSE248959
Raw and analyzed data: Polysome-seq	This paper	GEO: GSE248959
Raw and analyzed data: CUT&RUN-seq	This paper	GEO: GSE248959
Raw and analyzed data: RNA-seq PUS10 tdR-GLY-GCC/tdR-SCR-seq	This paper	GEO: GSE248959
Raw proteomic data (MS)	This paper	PDX061235
Experimental Models: Cell Lines		
MEFs hT *WT*	This paper	N/A
MEFs hT *Pus10-KO*	This paper	N/A
HEK293T	ATCC	RRID: CVCL_0045
WI38	ATCC	RRID: CVCL_0579

(*Continued on next page*)

Continued

REAGENT or RESOURCE	SOURCE	IDENTIFIER
Experimental Models: Organisms/Strains		
Mouse: Pus10−/− (*Pus10-KO*) C57/Bl6/SvJ	This paper	N/A
Mouse: C57/Bl6/SvJ	Lund University	N/A
Oligonucleotides		
Oligonucleotides are listed in Table S6	This paper	N/A
Recombinant DNA		
pLCV.2 TRE_Pus10 EF1alpha_rtTA_P2A_PuroCrRED	This paper	N/A
psPAX2	Addgene	#12260
pMD2.G	Addgene	#12259
pLVX-RNaseHI-NES-EGFP	Addgene	196701
1GFP/RNase H1 D210N	Addgene	174448
pCDH CMV-MCS-EF1-GFP-Puro	Systembio	CD513B-1#12259
Software and Algorithms		
Bowtie 1.2.2	Langmead et al.[95]	http://bowtie-bio.sourceforge.net/index.shtml
Piranha v1.2.1	Uren et al.[96]	http://smithlabresearch.org/software/piranha/
MEME	Bailey et al.[97]	https://meme-suite.org/meme/
MINTmap	Loher et al.[30]	https://github.com/stela2502/MINTmap
cutadapt v2.9	N/A	https://github.com/marcelm/cutadapt
GtRNAdb2	Chan & Lowe[98]	http://gtrnadb.ucsc.edu/GtRNAdb2/genomes/eukaryota/Hsapi38/hg38-tRNAs.fa
Seurat	Hao et al.[99]	https://satijalab.org/seurat/
Scanpy	Wolf et al.[100]	https://scanpy.readthedocs.io/en/stable/
TEtranscript	Jin et al.[40]	https://github.com/mhammell-laboratory/TEtranscripts
SnapGene	GSL Biotech LLC	https://www.snapgene.com/
GraphPad Prism version 9.0.0	GraphPad Software, Inc.	N/A
FACSDiva	BD Biosciences	N/A
FlowJo v10.9	BD Biosciences	N/A
STAR v2.7.8a	Dobin et al.[101]	https://code.google.com/archive/p/rna-star/
DESeq2	Love et al.[102]	https://bioconductor.org/packages/release/bioc/html/DESeq2.html
singscore	Foroutan et al.[103]	https://www.bioconductor.org/packages/release/bioc/html/singscore.html
GSEA v4.3.2	Subramanian et al.[104]	https://www.gsea-msigdb.org/gsea/index.jsp
Msstats	Huang et al.[105]	N/A
LIMMA	Smyth et al.[106]	N/A
ImageJ		https://imagej.nih.gov/ij/
Other		
BD FACS Aria III	BD Biosciences	N/A
BD LSR Fortessa	BD Biosciences	N/A
BD LSR Fortessa X20	BD Biosciences	N/A
BD LSRII	BD	N/A
Cytek Aurora	Cytek	N/A
Nikon Eclipse 2000 light microscope	Nikon	N/A
Amersham Hyperfilm ECL	GE Healthcare	28906837
UVP-1000 Crosslinker CL-1000	Analytik Jena	N/A
CFX96 qPCR	Bio-Rad	N/A
C1000 Touch thermocycler	Bio-Rad	N/A
ChemiDoc XRS+	Bio-Rad	N/A

(*Continued on next page*)

Continued

REAGENT or RESOURCE	SOURCE	IDENTIFIER
MiSeq sequencer	Illumina	N/A
NextSeq 500 sequencer	Illumina	N/A
Qubit® 2.0 Fluorometer	Thermo Fischer Scientific	N/A
2100 Bioanalyzer Instrument	Agilent	N/A
KX-21N	Sysmex	N/A
Orbitrap Exploris 480	Thermo Fischer Scientific	N/A
BioComp Gradient station	BioComp	N/A
Nikon Eclipse Ti2 microscope	Nikon	N/A
HiTrap Heparin HP affinity columns	GE Healthcare	17040701
HiTrap™ IMAC HP columns	GE Healthcare	17092003

EXPERIMENTAL MODEL AND SUBJECT DETAILS

Patients and samples

Human bowel biopsy samples from inflammatory bowel disease and control individuals were obtained from Hospital de Galdakao-Usansolo (Spain). An extra biopsy specimen was obtained in routine colonoscopy of the inflamed segment if present for individuals at high-risk of undiagnosed or for already diagnosed patients. None of the patients suffered from any other concomitant immunological disease. None of the controls showed intestinal inflammation at the time of the biopsy. This study was approved by the Basque Country Clinical Research Ethics Board (CEIm-E ref. PI2019133). Informed consent was received from all the patients and healthy donors. All experiments were performed in accordance with relevant guidelines and regulations.

Mouse strains

B6.SJL (CD45.1), C56Bl/6 (CD45.2) and C56Bl/6 x B6.SJL (CD45.1/CD45.2) mice used for transplantation assays were generated in-house. *Pus10KO* mice were generated by injecting 129; C57Bl/6 mouse embryonic stem cells harboring a Pus10-specific targeting vector (PRPGS00076_A_A04; EUCOMM) into a C57Bl/6N mouse blastocyst at the Core Facility for Transgenic Mice at University of Copenhagen. Mice were housed in individually ventilated cages (IVC) with 12-h light-dark cycles under controlled climate and enrichment environmental conditions with access to sterile food and water *ad libitum*. Sex was not considered as a biological variable. Mice aged between 11 and 20 weeks were used to test the effects of pro-inflammatory treatments, while overall survival was monitored for up to 100 weeks. All experimental procedures were approved by the Lund University Ethical Committee.

Cell culture

Mouse embryonic fibroblasts (MEFs) isolated from *WT* and *Pus10KO* mice were immortalized by transduction with hTERT-expressing retrovirus and cultured in DMEM (ATCC) supplemented with 10% fetal bovine serum (FBS, GE Healthcare) and 1% penicillin/streptomycin (Thermo Fisher). The cells were maintained on 0.1% gelatin-coated plates. Similarly, human WI38 cells (ATCC) were cultured in in DMEM (ATCC) supplemented with 10% fetal bovine serum (FBS, GE Healthcare) and 1% penicillin/streptomycin (Thermo Fisher). Overexpression of mouse Pus10 was obtained using a pLCV2 TetON doxycycline (DOX)-inducible lentiviral vector system carrying an N-terminal FLAG-tagged Pus10.[107] Cells were transduced with lentiviral particles and selected with puromycin (2 μg/mL). Pus10 expression was induced by addition of 2 μg/mL doxycycline (Sigma-Aldrich) for 48 h. A similar approach was used for lentiviral overexpression of an EGFP-tagged RNase H1[79] (Addgene #196701). Cells were grown at 37°C in humidified incubator at 5% CO_2, 20% O_2 and routinely tested for mycoplasma contamination.

METHOD DETAILS

Apoptosis analysis

Cells were stained with Annexin V conjugate (Thermo Fisher) and propidium iodide (Sigma)/DAPI suspensions in binding buffer containing 10 mM HEPES, 140 mM NaCl, and 2.5 mM $CaCl_2$ pH 7.4. Data was collected using a BD LSR Fortessa flow cytometer to measure Annexin V and propidium iodide levels. At least 20,000 events were recorded for each replicate and analyzed using FlowJo software. A 48 h dose-response curve was determined for *WT* and *Pus10KO* cells upon treatment with different concentrations of H-151 (Sigma). Viability was determined by MTT assay (Sigma).

Cell cycle analysis

Cell cycle was assessed by the staining of the bromodeoxyuridine (BrdU), incorporated into newly synthesized DNA, coupled with the staining of total DNA with 7-aminoactinomycin D (7-AAD), followed by the cytometric analysis. The assay was performed using BD

Pharmingen FITC BrdU Flow Kit following manufacturer's instructions (BD Biosciences). Briefly, cells were grown in the presence of BrdU at a final concentration of 10 μM in cell culture medium for 45 min. Subsequently, cells were fixed and permeabilized with BD Cytofix/Cytoperm Buffer for 30 min on ice and washed with 1× BD Perm/Wash Buffer. Following incubation with BD Cytoperm Permeabilization Buffer Plus for 10 min on ice, cells were washed with 1X BD Perm/Wash Buffer and re-fixed with BD Cytofix/Cytoperm Buffer for 5 min on ice. Then cells were washed with 1X BD Perm/Wash Buffer, treated with 300 μg/mL DNase/DPBS and washed with 1X BD Perm/Wash Buffer. Following 20 min incubation at room temperature with BD Perm/Wash Buffer containing antibodies against BrdU, cells were washed with 1× BD Perm/Wash Buffer and resuspended in 7-AAD solution in staining buffer prior to the analysis on using a BD LSR II, BD LSR Fortessa or BD LSR Fortessa X-20 flow cytometer. At least 10,000 events were analyzed using FlowJo software.

siRNA-mediated gene knockdown

For siRNA-mediated gene knockdown, MEFs and WI38 cells were transfected with 20 nM of control, cGAS and PUS10 pools of siRNA (Dharmacon) using RNAiMAX (Thermo Fisher) on the day of plating. cGAS and PUS10 downregulation was monitored by qPCR analysis at indicated experimental timepoints.

Transfection of synthetic tdRs

Transfection of tdRs was carried out using lipofectamine RNAiMAX reagent according to manufacturer's instruction. Briefly, MEFs were plated in gelatin-coated 6-well plates at a density of 0.5–1 × 10^5/well and transfected with 20 nM of tdR-5-GlyGCC or scrambled tdR-5 oligos (tdR-5-SCR). Cells were harvested 48 h after transfection and processed for Western blotting or RNA isolation. For experiments using human cells, WI38 cells were seeded at 1.5 × 10^5/well in a 6-well plate. The following day, cells were transfected with 20nM siCTR, 20nM siPUS10 alone or in combination with 20nM tdR-5-Gly-GCC, or 20nM tdR-5-SCR using lipofectamine RNAiMAX. Cells were harvested 48 h post-transfection. The list of oligo sequences is included in Table S9.

tdR quantification by SL-qPCR

tdR-5-GlyGCC quantification was performed using sequence-specific stem-loop primer for cDNA synthesis as described with some modifications.[9] Briefly, 200 ng of total RNA were treated with TURBO DNase (Thermo Fisher), denatured at 65°C for 5 min in the presence of 50 nM sequence-specific tdR-5-GlyGCC and mir16a stem-loop primers, 500 nM U6 reverse primer, 2.5 mM Oligo dT (Thermo Fisher) and 250 mM dNTPs (Thermo Fisher) final concentrations. Samples were transferred on ice for 2 min and 6.45 mL of retro transcription mix was added: 2.5 U/mL Superscript III (Thermo Fisher), 0.2 U/μL RNaseOUT (Thermo Fisher), 4 μL 5X First-Strand buffer (Thermo Fisher), 10 mM DTT (Sigma). cDNA synthesis was performed using the following protocol: 16°C for 30 min, 60 cycles at 30°C for 30 s, 42°C for 30 s and 50°C for 1 s. Finally, cDNA was diluted 1:4 in water and 1 μL subjected to qPCR using SsoAdvanced Universal SYBR Green Supermix (BioRad). The specificity of each amplification was validated by gel electrophoresis and sequencing. Primers are listed in Table S9.

Northern blot

Northern blot analysis was performed using 10 μg of total RNA on a 10% TBE-Urea gel (ThermoFisher). RNA was transferred to a Hybond-N+ membrane (GE Healthcare) and UV-crosslinked. The membrane was dried and pre-hybridized at 55°C for 30 min in PerfectHyb Plus Hybridization Buffer (Sigma) and 0.1 mg/mL herring sperm DNA (Thermo Fisher). Hybridization was performed in fresh hybridization buffer containing 1 × 10^6 cpm/ml of ^{32}P-labeled tRNA-GlyGCC probe and 0.1 mg/mL herring sperm DNA (Thermo Fisher) at 55°C overnight. Subsequently, the membrane was washed once in low stringency buffer (2× SSC, 0.1% SDS) at room temperature for 5 min and twice in high stringency buffer (0.5× SSC, 0.1% SDS) at 42°C for 20 min. Quantification was performed overnight using a phosphorimager (Fuji film FLA3000). After exposure the membranes were incubated in boiling stripping buffer (0.1% SDS, 5 mM EDTA) and probed for U6 for loading control as described. Probe sequences are listed in Table S9.

RT-qPCR

RNA was extracted using TRIzol reagent (Thermo Fisher) and Direct-Zol RNA kit (Zymo Research) and DNAse-treated using the Direct-Zol RNA kit (Zymo Research) following manufacturers' instructions. For small RNA detection, DNAase treatment was performed using the TURBO DNA-free Kit (Thermo Fisher). RNA concentration was measured using Nanodrop ND-1000. For small RNA detection, 0.2–0.5 μg of RNA was retrotranscribed using miScript II RT Kit (Qiagen) in a 10 μL reaction (5× miScript HiFlex Buffer, 10x miScript Nucleics Mix, 1 μL miScript Reverse Transcriptase Mix) for 60 min at 37°C, 5 min at 95°C. For all the other applications, 0.5–1 μg of RNA was retro-transcribed using the High-Capacity cDNA Reverse Transcription Kit (Thermo Fisher) in a 20 μL reaction (10× RT Buffer, 10× RT Random Primers, 25× dNTP Mix (100 mM), 1μL MultiScribe Reverse Transcriptase (50 U/μL), 1μL RNase Inhibitor) for 10 min 25°C, 2 h 37°C, 5 min 85°C. cDNA was diluted 1:5 in water and immediately used for RT-qPCR or stored at −20°C. RT-qPCR was performed using SsoAdvanced Universal SYBR Green Supermix (BioRad) in an 8 μL reaction (2× SYBR Green Supermix, 200nM forward and reverse primers, 1 μL of diluted cDNA). Quantification was performed using CFX96 Real-Time System with C1000 Thermal Cycler (Bio-Rad) with the following protocol: 95°C for 5 min, 35 cycles of 95°C 10s and 60°C 30 s with signal acquisition. Melting curves were evaluated from 65°C to 95°C with increments of 0.5°C for 5 s and signal acquisition. The C_q was determined by regression method using the CFX Manager Software (Bio-Rad). The RT-qPCR reaction was performed in technical

duplicate and the average C_q was used to calculate the relative expression using the $2^{-\Delta\Delta CT}$ method in Microsoft Excel. Patient biopsies were homogenized using a pellet pestle. RNA was extracted using Nucleospin RNA Mini Kit (Macherey Nagel) and used for One Step RT-QPCR using the One-step NZYSpeedy RT-qPCR Green kit with specific primers. The complete list of primers used in this study is provided in Table S9.

Measurement of RIG-I-like receptors (RLRs) activity

IFN-β promoter-luciferase reporter activity in the Tet-on 293 cells expressing RIG-I or MDA5 as previously described.[42] Cells were stimulated with 10 μg/mL of poly I:C or total RNA from WT and Pus10KO cells for 16 h, followed by the measurement of IFN-β promoter-luciferase reporter activity. In each experiment, RIG-I or MDA5 expression was induced by 1 μg/mL doxycycline 8 h prior to stimulation.

Expression and purification of GFP-dRNase H1 D210N (GFP-dRH)

GFP tagged, catalytically inactive RNAse H1 was prepared using the GPF/RNase H1 D210N (GFP-dRH) vector (Addgene #174448) and purified as previously described[44] with some modifications. Briefly, the protein was expressed in Escherichia coli BL21(DE3) cells (Thermo Fisher) in LB medium and induced with IPTG overnight at 20°C. The cells were lysed by sonication in buffer containing 50 mM Tris pH 7.5, 500 mM NaCl, 5% glycerol and 10 mM Imidazole supplemented with protease inhibitors (Roche), 1 mg/mL lysozyme and 5 μg/mL DNaseI (GE Healthcare). The proteins were isolated from the cleared lysate by binding to a Nickel-charged HiTrap IMAC column (GE Healthcare) and eluted from the column by a linear gradient to the same buffer supplemented with 500 mM imidazole. Subsequently, the protein was diluted to have a salt concentration of 100 mM NaCl and loaded on a HiTrap Heparin column (GE Healthcare) equilibrated with buffer containing 50 mM Tris pH 7.5, 100 mM NaCl, 5% glycerol and 2 mM DTT and eluted from the column by a linear gradient to the same buffer supplemented with 1M NaCl. The fractions containing the protein were pooled and buffer exchanged into 50 mM Tris pH 7.5, 250 mM NaCl, 0.3% NP40, 10% glycerol and 1 mM DTT and flash frozen in liquid nitrogen.

Imaging RNA-DNA hybrids with recombinant GFP-dRH

Imaging of GFP-dRH was performed as described with some modifications. Briefly, cells were washed once with PBS, fixed in ice-cold methanol (Sigma) for 5 min at −20°C, washed twice with PBS, and permeabilized with 0.25% Triton X-100 (Sigma) for 3 min. Next, cells were washed twice with PBS and blocked with staining buffer [3% BSA (Sigma) in PBS with 0.1% Tween (PBST, Sigma)] for 30 min. Samples were incubated with a 1:2000 dilution of GFP-dRH at 0.190 mg/mL in staining buffer for 2 h at 37°C. After washing thrice with PBST for 5 min, cells were counterstained with DAPI 5 ng/mL (Thermo Fisher) in PBS for 10 min, wash thrice in PBS for 5 min, and coverslips mounted on glass slides using Prolong Gold antifade (Thermo Fisher). Slides were stored at 4°C in the dark until imaging. Microscopy images were acquired using a Nikon Eclipse Ti2 microscope in widefield mode with a 100 ×1.45 NA objective and a Nikon DS-Qi2 CMOS camera and a LED light source. Image acquisition parameters such as LED power and camera exposure times were kept constant across conditions. Post acquisition, image processing and analysis was carried out in FIJI and Cell Profiler software. Briefly, individual channels were background subtracted in FIJI using the rolling ball algorithm. Cell Profiler was then used to segment the nuclear and FITC/GFP (whole cell) channel. The cytoplasmic region was identified by subtracting the segmented whole cell image from the segmented nuclear image and the total intensities in the 2 regions were subsequently calculated.

Western blotting

Cells were washed with ice-cold PBS and lysed in ice-cold RIPA lysis buffer (50 mM Tris-HCl pH 8, 150 mM NaCl, 0.5% sodium deoxycholate, 0.1% sodium dodecyl sulfate, 0.5% Triton X-100, 0.5 mM EDTA, pH 8) supplemented with protease inhibitor cocktails (Sigma) and freshly prepared phosphatase inhibitor cocktail (Roche, Sigma). Lysates were cleared by centrifugation at 15000 rpm for 10 min at 4°C. The supernatants were collected and assayed for protein concentration using the Pierce BCA Protein Assay Kit (Thermo Fischer). Lysates were denatured by the addition of 5× Laemmli sample buffer (1% sodium dodecyl sulfate, 300 mM Tris-HCl pH 8, 50% glycerol, 0.025% bromophenol blue and 10% 2-mercaptoethanol) and incubation for 5 min at 95°C. At least 40 μg of protein lysates were subjected to SDS-PAGE and transferred to PVDF membranes (Bio-Rad) following the manufacturer's instructions followed by blocking in 3% BSA in PBS supplemented with 0.1% Tween 20 (PBST). Incubation with primary antibodies was carried out overnight at 4°C. Select tissues were harvested from mice and snap frozen. Samples were cold processed using tissue pulverizer (BioSpec) and protein was isolated and processed as described above. A list of antibodies used is included in the key resources table.

Global measurement of protein synthesis

Protein synthesis rate was determined using [^{35}S] radioactive metabolic labeling as previously described.[9] Cells were starved for 30 min in methionine- and cysteine-free DMEM medium supplemented with 10% dialyzed FBS. Cells were then treated with a 30 μCi/mL protein labeling mix (EasyTag Protein Labeling Mix, PerkinElmer) for 30 min. After treatment, cells were harvested, lysed in RIPA buffer, and equal amounts of total proteins were separated on a 10% SDS polyacrylamide gel and transferred to PVDF membranes. Membranes were exposed to autoradiography film (GE Healthcare) at −80°C overnight and imaged. The incorporation of ^{35}S-methionine/cysteine was quantified using Image Lab software and normalized to a loading control.

Polysome fractionation

Polysomal fractionation was performed as described previously.[9] Briefly, *WT* or *PUS10KO* MEFs were cultured in 10cm dishes to have them at approximately 70–80% confluency on the day of the experiment. Cells were incubated for 10 min at 37°C in media supplemented with 10 μg/mL cycloheximide (CHX) (Sigma-Aldrich). After washing with ice-cold PBS containing 10 μg/mL CHX cells were lysed in 450 μL polysome lysis buffer (PLB) with 10 mM Tris-HCl pH 8.0, 150 mM NaCl, 1.5 mM $MgCl_2$, 0.25% NP-40, 0.1% Triton X-100, 320 U/mL SUPERase-In RNase Inhibitor (Thermo Fisher), 150 μg/mL CHX (Sigma-Aldrich) and 20 mM DTT. Lysates were incubated on ice for 40 min, mixed every 10 min and cleared at 15,000 rpm for 10 min at 4°C. Equal amounts of lysates were layered onto a linear 10%–60% sucrose (Thermo Fisher) (w/v) gradients in 25 mM Tris-HCl pH 7.4, 25 mM NaCl, 5 mM $MgCl_2$, 0.1 mg/mL heparin and 2 mM DTT in nuclease-free water. Samples were centrifuged using a SW41Ti rotor (Beckman) for 2.5 h at 37,000 rpm at 4°C and fractioned using a BioComp Gradient Station (BioComp). To each 650 μL fraction, 800 μL of TRIzol was added and samples were immediately snap-frozen on dry ice. For individual sucrose gradient fractions, RNA isolation was carried out using Direct-Zol RNA Miniprep (Zymo Research) with the in-column DNAse treatment according to manufacturer's protocol. For normalization, 5 ng of an in vitro-transcribed luciferase RNA was added to each sample before RNA isolation. Sequencing libraries were generated using 500 ng of total or polysomal RNA with the TruSeq Stranded Total RNA Library Prep Kit (Illumina) according to the manufacturers' instructions. Libraries were sequenced on an Illumina NovaSeq 6000 with paired end 150 cycles.

tdR-5-GlyGCC pulldowns

Identification of tdR-5-GlyGCC interacting proteins was performed as described with some modifications.[9] One sub-confluent 10 cm plate of *WT* or *PUS10KO* cells were transfected with 20 nM of either biotinylated scramble oligo or tdR-5-Gly GCC using RNAiMAX reagent (Thermo Fisher). 24 h post transfection, cells were washed with PBS and UV-crosslinked at 254nm with 200 mJ/cm^2 and harvested on ice. Cell pellets were lysed in Lysis Buffer [50 mM Tris/HCl pH 7.4, 100 mM NaCl, 0.5% Triton X-100, 0.5% sodium deoxycholate, 0.1% SDS, 5 mM EDTA, 0.1 U/uL supplemented with RNase inhibitors (Thermo Fisher) and protease inhibitors (Sigma-Aldrich)]. Lysates were sonicated 3 × 10 s at 10 W and cleared by centrifugation. Cleared extracts were incubated with pre-washed streptadivin-C1 dynabeads (Thermo Fisher) for 1 h at 4°C, rotating. After incubation beads were washed twice in Lysis buffer, twice in High-salt buffer (50 mM Tris/HCl, 1000 mM NaCl, 0.5% Triton X-100, 0.25% sodium deoxycholate, 1 M Urea, 5 mM EDTA, 1 mM DTT), and twice in PNK/Tween buffer (50 mM Tris/HCl, 10 mM $MgCl_2$, 0.2% Tween 20). For recovery of proteins, samples were pre-digested on-bead in 50 mM ammonium bicarbonate (Sigma) with 0.1% RapiGest (Waters), 1 mM dithiothreitol and 400 ng sequencing grade modified trypsin (Promega) for 2 h at 37 °C with gentle rotation. The resulting peptide-containing supernatant was collected and reduced further with 0.1 M dithiothreitol at 56°C, alkylated with 0.2 M iodoacetamide at room temperature, and digested overnight at 37°C with trypsin (enzyme: protein ratio 1:50). Digested peptides were acidified with 10% trifluoroacetic acid and RapiGest was precipitated by incubation at 37°C. Peptides were desalted with in-house C18 stage tips, dried by vacuum centrifugation, and resuspended in Mass Spectrometry (MS) loading buffer (4% acetonitrile in 0.1% (v/v) formic acid) prior to LC-MS analysis.

Liquid chromatography and mass spectrometry (LC-MS)

LC-MS analyses were carried out on an Orbitrap Exploris 480 MS instrument equipped with FAIMS Pro, coupled to a reverse phase UltiMate 3000 UHPLC system and an EASY-Spray ion source (all Thermo Fisher). Peptides samples were measured with data-independent acquisition (DIA). Digested peptides were loaded onto a trap cartridge (Acclaim PepMap C18, 5 mm particle size, 0.3 mm inner diameter x 5 mm length, Thermo Fisher) and separated by EASY-Spray analytical column (2 mm particle size, 75 mm inner diameter x 500 mm length (Thermo Fisher). The mobile phases for LC separation were 0.1% (v/v) formic acid in LC-MS grade water (Solvent A) and 0.1% (v/v) formic acid in 80% acetonitrile (Solvent B). Each sample was injected once and eluted at a constant flow rate of 300 nL/min at 45 °C with a linear gradient ranging from 2 to 19% Solvent B over 80 min, 19–41% Solvent B over 40 min, 41–90% Solvent B over 5 min and finally 90–95% Solvent B over 5 min. The spray voltage was set at 2.1 kV, ion transfer tube temperature was set at 275°C, and FAIMS compensation voltages (CV) were set to −45 and −60. For DIA analysis, peptides were analyzed with one full scan (350–1,400 m/z, R = 120,000) at a normalized AGC target of 300%, followed by 38 DIA MS/MS scans (350–1,050 m/z) in HCD mode (isolation window 18 m/z, 1 m/z window overlap, normalized collision energy 27%), with fragments detected in the Orbitrap (R = 15,000). All data were acquired in positive polarity and MS/MS were acquired in centroid mode.

CUT&RUN

CUT&RUN was performed as described elsewhere[41] with some modifications. Briefly, 5 × 10^5 *WT* and *Pus10KO* cells were washed twice (20 mM HEPES pH 7.5, 150 mM NaCl, 0.5 mM spermidine, 1× Roche cOmplete protease inhibitors) and attached to 10 μL (per cell line per antibody) ConA-coated magnetic beads (Bangs Laboratories) that had been pre-activated in binding buffer (20 mM HEPES pH 7.9, 10 mM KCl, 1 mM $CaCl_2$, 1 mM $MnCl_2$). Cells were then resuspended in 50 μL buffer (20 mM HEPES pH 7.5, 0.15 M NaCl, 0.5 mM Spermidine, 1× Roche complete protease inhibitors, 0.05% w/v digitonin, 2 mM EDTA) containing 1:50 dilution of the primary antibody (goat anti-rabbit IgG (Abcam, CAT#ab97047), rabbit anti-H3K4me3 (Active motif CAT#39159) and incubated at 4 °C overnight. Beads were washed thoroughly with digitonin buffer (20 mM HEPES pH 7.5, 150 mM NaCl, 0.5 mM Spermidine, 1× Roche cOmplete protease inhibitors, 0.05% digitonin). After the last wash, pA-MNase (a generous gift from Steve Henikoff) was added in digitonin buffer and incubated with the cells at 4 °C for 1 h. Bead-bound cells were washed twice, resuspended in

100 μL digitonin buffer, and chilled to 0–2°C. Genome cleavage was stimulated by addition of 2 mM $CaCl_2$ at 0 °C for 30 min. The reaction was quenched in 100 μL 2 stop buffer (0.35 M NaCl, 20 mM EDTA, 4mM EGTA, 0.05% digitonin, 50 ng/mL glycogen, 50 ng/mL RNase A and vortexing. After 10 min incubation at 37°C to release cleaved fragments, cells and beads were pelleted by centrifugation (16,000 × g, 5 min, 4°C) and the supernatant purified by a PCR clean-up kit (Macherey-Nagel). Illumina sequencing libraries were prepared using the Hyperprep kit (KAPA) with unique dual indexed adapters (KAPA), pooled and sequenced on a Nextseq500 instrument (Illumina).

RNA-seq

Total DNA-free RNA was isolated from MEFs using the Quick-RNA Miniprep Kit (Zymo Research). RNA quality was assessed by Bioanalyzer RNA 6000 Nano assay (Agilent). 250 ng of total RNA was used for library preparation. Single-indexed libraries were prepared using the Low Sample (LS) Protocol of TruSeq Stranded Total RNA Library Prep Gold (Illumina) according to manufacturer's instructions. Library quality was verified by Bioanalyzer High Sensitivity DNA Analysis (Agilent). Sequencing was carried out on the Illumina NextSeq 500 System in a paired-end approach using NextSeq 500/550 High Output v2 kit (Illumina). For LSK, total RNA integrity was determined using Agilent Bioanalyzer. Library preparation was performed with 10 ng of total RNA with a Bioanalyzer RIN score greater than 8.0. ds-cDNA was prepared using the SMARTer Ultra Low RNA kit for Illumina Sequencing (Takara-Clontech) per the manufacturer's protocol. cDNA was fragmented using a Covaris E220 sonicator using peak incident power 18, duty factor 20%, cycles per burst 50 for 120 s cDNA was blunt-ended, had an A base added to the 3′ ends, and then had Illumina sequencing adapters ligated to the ends. Ligated fragments were then amplified for 12–15 cycles using primers incorporating unique dual index tags. Fragments were sequenced on an Illumina NovaSeq-6000 using paired end reads extending 150 bases. For the RNA sequencing upon transfection with the tdR-5-GlyGCC/SCR, *PUS10KO* cells were plated in gelatin-coated 10cm plates at a density of 1×10^6 cells and transfected with 20 nM of tdR-5-GlyGCC or tdR-5-SCR. Cells were harvested and lysed in TRIzol 24h post transfection. RNA was isolated using the Quick-RNA Miniprep Kit (Zymo Research). Sequencing libraries were generated using 500 ng of total RNA with the TruSeq Stranded Total RNA Library Prep Kit (Illumina) according to the manufacturers' instructions. Libraries were sequenced on an Illumina NovaSeq 6000 with paired end 150 cycles.

Small RNA-seq

Total DNA-free RNA was isolated using Quick-RNA Miniprep Kit (Zymo Research). RNA quality assessment by Bioanalyzer RNA 6000 Nano assay (Agilent), libraries were prepared using NEXTFLEX Small RNA-Seq Kit v4 (PerkinElmer) according to manufacturer's instructions. Briefly, 2 mg of total RNA was used for library preparation. Following non-diluted adapters ligation and reverse transcription - first strand synthesis, 20 cycles of PCR amplification were performed. The PCR product was purified using a gel-free size selection method. Library quality was verified by Bioanalyzer High Sensitivity DNA Analysis (Agilent). Sequencing was carried out on the Illumina NextSeq 500 System for 75 cycles in a single-read approach using NextSeq 500/550 High Output v2 kit (Illumina).

iCLIP-seq

iCLIP-seq was performed as described previously.[9] In brief, 10 000 000 MEFs were crosslinked with UV light (200 mJoule/cm2 at 254 nM; UVP crosslinker, Analylitk Jena), harvested and lysed in iCLIP lysis buffer (50 mM Tris HCl pH 7.4, 100 mM NaCl, 0.5% Triton X-100, 0.5% sodium deoxycholate, 0.1% SDS, 5 mM EDTA) supplemented with protease inhibitors (Sigma) and sonicated three times with 10 s bursts at 20 W (Branson). Following treatment with 5 U/mL RNase I (Thermo Fisher) and 1 U/mL TURBO DNase (Thermo Fisher) for 3 min at 37°C shaking at 1100 rpm, lysates were cooled down on ice for 5 min, centrifuged at 15000 rpm for 10 min at 4°C and supernatants were collected. Supernatants were incubated and pre-washed with Protein A Dynabeads (Life Technologies) coated with anti-Pus10 antibody for 2 h at 4°C rotating, washed with lysis buffer, and RNase I was added for 5 min at 37°C shaking at 1100 rpm. The reaction was blocked by the addition of high-salt buffer (50 mM Tris HCl, 1000 mM NaCl, 0.5% Triton X-100, 0.25% sodium deoxycholate, 1 M urea, 5 mM EDTA, 1 mM DTT). Subsequently, samples were washed twice with high-salt buffer at 4°C, once with PNK/Tween buffer (20 mM Tris HCl pH 7.4, 10 mM MgCl2, 0.2% Tween 20) and once with wash buffer (50 mM Tris/HCl pH 7.4, 10 mM MgCl2). Samples were resuspended in 20 μL PNK dephosphorylation mix (4 μL 5× PNK buffer pH 6.5 (350 mM Tris-HCl pH 6.5, 50 mM MgCl2, 5 mM DTT), 0.5 μL T4 PNK (NEB), 0.5 μL SUPERase-IN RNase Inhibitor (Thermo Fisher) and incubated 15 min at 37°C. Following wash with high-salt buffer and two washes with wash buffer, samples were resuspended in 20 μL of L3 adaptor ligation mix (2 μL 10× T4 RNA ligation mix (NEB), 1 μL T4 RNA ligase I (NEB), 0.5 μL SUPERase-IN RNase Inhibitor (Thermo Fisher), 1.5 pmol pre-adenylated L3 linker, 4 μL PEG400) and incubated overnight at 16°C shaking. Samples were washed twice with high-salt buffer, once with wash buffer, radiolabeled with 20 μL of T4 PNK mix containing 2 μL of 10X T4 PNK Buffer (NEB), 1 μL T4 PNK (NEB), 0.5 μL γ-32P-ATP (PerkinElmer) for 5 min at 37°C shaking at 1100 rpm and further washed once in HS and twice in PNK/Tween buffers. Beads were resuspended in 20 μL of 1.5× Nu-PAGE loading buffer (Thermo Fisher) and incubated for 10 min at 70°C shaking at 1100 rpm. Then, collected supernatant was added to 1 μL 1 M DTT and boiled 3 min at 95°C. Samples were separated by NuPAGE 4%–12% Bis-Tris gel (Thermo Fisher) electrophoresis and transferred onto a 0.45 μm nitrocellulose membrane (GE Healthcare). Membrane fragments containing protein-RNA complexes were excised and incubated with PK buffer for 30 min at 37°C shaking at 1100 rpm. Reactions were stopped by adding an equal amount of PK buffer supplemented with 7 M urea. RNA was extracted using Phase Lock Gel Heavy tube (VWR) and ethanol-precipitation. cDNA synthesis was performed using Superscript III (Thermo Fisher). cDNA was circularized using CircLigase II (Epicenter), annealed with 0.25 μM Cut oligo and digested with BamHI

(Thermo Fisher). Digested cDNA was ethanol-precipitated and resuspended in 21 μL of water. 1 μL of cDNA was used for PCR amplification using Accuprime Supermix I with 18–21 PCR cycles. Sequencing was carried out on the Illumina NextSeq 500 System in a single-read approach.

RNA dot blot

Isolation of nuclear and cytoplasmic RNA was performed using the Cytoplasmic and Nuclear RNA Purification Kit (Norgen Biotek). Briefly, RNA (1 μg) was incubated for 3 min at 95°C to disrupt secondary structures and immediately chilled on ice, and 2 μL spotted onto a positively charged nylon membrane (Amersham). RNA was crosslinked to the membrane with UV light (125 mJ/cm^2 at 254 nM; UVP crosslinker, Analytik Jena). The membrane was washed with TBST (1× TBS, 0.1% Tween 20), and non-specific binding was blocked with 5% skimmed milk (blocking buffer). Following overnight incubation in primary antibody diluted in blocking buffer at 4°C, the membrane was washed with TBST and incubated in secondary antibody solution in blocking buffer for 1 h at room temperature. The membrane was washed with TBST and imaged with ChemiDoc XRS+. Ultimately, the membrane was stained in methylene blue (0.2% methylene blue in 0.4M sodium acetate and 0.4M acetic acid) staining buffer for 30 min at room temperature to determine RNA loading and washed with distilled water before imaging. S9.6 staining specificity was assessed by treating 1 μg of RNA with RNase H (NEB) or RNase III (Ambion) for 1 h at 37°C, following the manufacturer's instructions, and heat-inactivating the enzymes before spotting.

Bleeding and isolation of bone marrow cells

Peripheral blood was sampled from the tail vein into 2% FBS/PBS supplemented with heparin (Leo Pharma, 10 IE/ml). For BM cell isolation, femurs, tibias and hip bones were collected from both hind legs and crushed with a mortar and a pestle in ice-cold 2% FBS/PBS. Single-cell suspensions were filtered through 40 μm cell strainers prior to downstream processing. Complete cell count was determined using Sysmex KX-21N (Sysmex).

Flow cytometric analysis

For peripheral blood (PB) analysis, erythrocytes were sedimented with 1% Dextran T500 (Sigma-Aldrich) at 37°C for 30 min, and the remaining erythrocytes were lysed using ammonium chloride solution (STEMCELL Technologies) for 3 min at room temperature. The cells were stained in 2% (v/v) FBS/PBS with 2 mM EDTA (VWR) with antibodies against B220 (BioLegend; CAT#103224), Gr-1 (BioLegend; CAT#108407), CD11b (BioLegend; CAT#101208) and CD3 (BioLegend; CAT#100214) (PB analysis of adult mice) or Gr-1 (BioLegend; CAT#108407), CD19 (Sony; CAT#1177600), CD3 (Sony; CAT#1101080), CD11b (Sony; CAT#1106060), NK-1.1 (Sony; CAT#1143610), CD45.1 (Sony; CAT#1153680) and CD45.2 (Sony; CAT#1149195) (PB analysis after transplantation). For HSPCs analysis, BM cells were incubated with Fc block (BD Pharmingen; CAT#553142) for 15 min on ice, followed by staining with antibodies against lineage markers (B220 (BioLegend; CAT#103210), Gr-1 (BioLegend; CAT#108410), CD3e (BioLegend; CAT#100310), TER-119 (BioLegend; CAT#116210)), CD117 (BioLegend; CAT#105812), Sca-1 (BioLegend; CAT#108114), CD48 (BioLegend; CAT#103432) and CD150 (BioLegend; CAT#115927) (BM analysis of adult mice) or against lineage markers (B220 (BioLegend; CAT#103210), Gr-1 (BioLegend; CAT#108410), CD3e (BioLegend; CAT#100310), TER-119 (BioLegend; CAT#116210), NK-1.1 (BioLegend; CAT#108716)), CD117 (Invitrogen; CAT#47-1171-82), Sca-1 (BioLegend; CAT#122520), CD48 (BioLegend; CAT#103404), CD150 (BioLegend; CAT#115914), CD201 (Invitrogen; CAT#17-2012-82), CD135 (Sony; CAT#1276530), CD127 (Sony; CAT#1275030), CD45.1 (Sony; CAT#1153680) and CD45.2 (Sony; CAT#1149195) (BM analysis after transplantation). Following staining, cells were washed and incubated with Qdot 605 Streptavidin Conjugate (Invitrogen; CAT# Q10101MP)) for 30 min on ice (BM analysis after transplantation). Staining mixes containing antibodies conjugated to Brilliant Violet dyes were supplemented with 10% Brilliant Stain Buffer Plus (BD). Before analysis, the cells were stained with propidium iodide (1:1000, Sigma-Aldrich) to mark dead cells. The cells were analyzed by flow cytometry on LSR Fortessa or Fortessa X20 instruments (Becton Dickinson). Data were analyzed using FlowJo 10 software (version 10.9, BD). HSPC subpopulations were defined based on the following phenotypes: HSC: Lineage-Sca-1+cKit+ (LSK) CD150+CD48$^-$CD201+, MPP1: LSK CD150-CD48$^-$, MPP2: LSK CD150+CD48$^+$, GMLP: LSK CD150-CD48$^+$ and CLP: LSK CD127+CD135+.

Poly I:C treatment

Adult (11-20-week-old) male and female *WT* and *Pus10KO* mice were intraperitoneally (i.p.) injected with Poly I:C HMW (InvivoGen) at 10 mg/kg for 6 consecutive days. Untreated mice served as controls. One day following the last injection, the mice were sacrificed and used as donors for transplantation experiment.

Transplantation

All transplantations were performed through intravenous tail vein injection into young (2–4 months) lethally irradiated (9 Gy) recipients. For primary transplantation, 1×10^6 BM cells from untreated or poly I:C-treated *WT* and *Pus10KO* mice were injected alongside 2×10^6 bone marrow cells from B6.SJL mice into B6.SJL recipients. For secondary transplantation, 5x10^6 whole BM cells from primary recipients were injected into C57BL/6xB6.SJL secondary hosts. The mice received antibiotic prophylaxis (Ciprofloxacin, HEXAL, 125 mg/L in drinking water) for two weeks following irradiation.

DSS colitis

Colitis in mice was induced by providing 1.5% (w/v) dextran sodium sulfate (DSS) (Merck) dissolved in drinking water *ad libitum* for 7 days, followed by 7 days of regular water. Female mice (15-19-week-old) were monitored daily for health and body weight. At specified time points, colons from DSS-treated mice were harvested, measured, and processed.

Colonic lamina propria (cLP) cell isolation and flow cytometry

cLP was prepared as described with some modifications.[66] Briefly, the colon was removed from the mice and flushed with HBSS (Gibco) with HEPES (pH 7.4, Gibco) to remove feces. Fat and the caecum were removed, and the organ was opened longitudinally, then sliced into 1 cm portions. To remove epithelial cells the organ was then incubated for 3 × 15 min at 37°C in HBSS with 10% FBS and EDTA 2 mM. After each incubation the tube was shaken for 10 s and waste epithelial cells, debris and media were then discarded by filtering through a nylon filter (250 μm). The tissue was then flushed with HBSS/HEPES pH 7.4 to remove EDTA and then incubated for 40 min at 37°C, 5% CO_2 on a magnetic stirring plate in R10 cell culture media (RPMI 1640, 10% FCS, 10 mM HEPES (pH 7.4), sodium pyruvate (20 mM, Gibco), 100 U/mL penicillin, streptomycin (100 μg/mL, Sigma Aldrich), gentamycin (50 μg/mL, Gibco) and β-mercaptoethanol (0.05 mM, Gibco), DNase (30 μg/mL, Roche) and Liberase TM (0.3 U/mL, Roche), to digest the extracellular matrix of tissue and release single cells for analysis. The remaining cell suspension was then filtered through 70 μm cell strainer (Fischer Scientific) and then 40μm. The remaining single cell suspension was then centrifuged, and pellets were resuspended in FACS buffer ready for antibody staining. Data were collected for this study using Cytek Aurora (Cytek) spectral flow cytometer and analyzed on FlowJo 10 software. To block Fc receptor the cells were incubated with CD16/32 for 15 min. Surface staining of desired antibodies (Fluorochrome-conjugated monoclonal antibodies specific for CD11b (clone M1/70), CD45 (clone 30-F11), Ly6G (clone 1A8), TCRβ (clone H57-597), CD19 (clone 1D3) all purchased from, eBioscience, Biolegend or BD Bioscience) was performed at 4°C for 30 min. The cells were then fixed and permeabilized with eBioscience Foxp3/transcription Factor Staining Buffer Set. The cells were washed in permeabilization buffer and pellets were resuspended in FACS buffer, ready for analysis. Aggregates and doublets were excluded from analyses using FSC-A versus FSC-H. Dead cells were identified LIVE/DEAD Blue Fixable Dead Cell Staining Kit (Thermo Fischer).

QUANTIFICATION AND STATISTICAL ANALYSIS

Unless otherwise stated, data is presented as mean, ±SD or SEM. At least three independent biological replicates have been performed for each experiment. The number of independent experiments is indicated. Statistical tests used and *p* values are indicated in figures and figure legends, unless otherwise stated. No statistical method was used to predetermine the sample size.

RNA-seq data analysis

RNA-seq datasets were aligned to the mm10 annotation of the mouse genome using STAR v2.7.8a[101] with the parameter outFilterMultimapNmax set to 1. Bioconductor package DESeq2[102] was used to analyze differential gene expression. Gene expression levels, $\log_2$ of normalized counts by DESeq2, were used as input of GSEA v4.3.2[104] for gene set enrichment analysis. The raw reads from LSK sequencing were trimmed from the 3′ adaptor sequence (AGATCGGAAGAG) by cutadapt v2.9 before differential expression, gene set enrichment and transposable element analysis (see below).

iCLIP-seq data analysis

The reads were classified into samples according to sample-specific barcodes. The barcodes and UMIs, 5 nucleotide unique sequence identifiers introduced during RT step, were removed and appended to the read name using UMI-tools.[108] The sequences were trimmed the 3′ adaptor sequence (AGATCGGAAGAGCGGTTCAG) by cutadapt v2.9 with parameter -m set to 18 and mapped to mouse genome mm10 using STAR[101] with the following parameters: –outFilterMismatchNoverReadLmax 0.04 –outFilterMismatchNmax 999 –outFilterMultimapNmax 1 (unique mapping) or –outFilterMultimapNmax 100 (multiple mapping). PCR duplicates were removed based on UMIs using UMI-tools. Peak identification was performed using Piranha v1.2.1,[96] and motif analysis was performed using the MEME.[97] The peaks were annotated using Gencode vM25, miRBase and GtRNAdb2.[109]

Small RNA-seq analysis

The raw sequence data were trimmed in the 3′ adaptor sequence (TGGAATTCTCGGGTGCCAAGG) by cutadapt v2.9. The sequence reads were aligned to an rRNA reference using Bowtie v.1.2.2.[95] The unaligned reads were collected and the rRNA alignments were discarded to reduce rRNA contamination. For tRNA analysis, Bowtie was used to map the reads to tRNA sequences from GtRNAdb2 (http://gtrnadb.ucsc.edu/GtRNAdb2/genomes/eukaryota/Hsapi38/hg38-tRNAs.fa). The data was quantified using samtools idxstats and read counts generated for each tRNA isoacceptor were combined. For tdR analysis, the reads were annotated using MINTmap software.[30] Each fragment sequence was grouped according to tRNA isoacceptor, origin (5′, 3′ or internal) and length (fragment or half) according to MINTmap annotation. DESeq2 was used to determine differentially expressed tdRs in *WT* and *Pus10KO* cells.

Transposable element analysis

RNA-seq datasets were aligned to the mouse genome mm10 using STAR. Reads were allowed to map to 1 locus (unique mapping) or 100 loci (multiple mapping). Read quantification was performed using TEtranscript[40] and TElocus (https://github.com/mhammell-laboratory/TElocal). DEseq2 was used to perform differential expression analysis.

CUT&RUN analysis

All paired-end reads were aligned to the mouse genome sequence using hisat2 program with parameters –no-mixed –no-discordant –no-spliced-alignment, and peaks for H3K4me3 were called using MACS2 from bam files. Signal profiles of H3K4me3 were plotted by deepTools.

Polysome-seq analysis

The raw reads were trimmed from the 3′ adaptor sequence (AGATCGGAAGAG) by cutadapt and mapped to the mouse genome using STAR with the parameters "–outFilterMultimapNmax 1" for obtaining the uniquely mapped reads, "–twopassMode Basic" for using the two-pass mapping mode, and "–quantMode GeneCounts" for counting number of reads per gene. Differential expression at transcription and translation levels and translation efficiency analyses were performed using the Bioconductor package DESeq2 with an interaction term model and the in vitro-transcribed luciferase RNA for size factor estimation. Genes with an adjusted p-value <0.05 and absolute value of log2FoldChange ≥ 1, ≥ 0.7 were considered for differential transcription, and translation, respectively.

MS raw data processing and statistical analysis

The MS data were searched with 'directDIA' in Spectronaut (version 18, Biognosys AG) against the Uniprot mouse reference proteome (21,717 entries downloaded in May 2024) together with commonly observed contaminants. Searches used carbamidomethylation as fixed modifications, methionine oxidation, and protein N-terminal acetylation as variable modifications. The Trypsin/P proteolytic cleavage rule was used, permitting a maximum of 2 missed cleavages and a minimum peptide length of 7 amino acids. Data filtering was set to Q-value and the Q-value thresholds were set to 0.01 at PSM, peptide, and protein levels. Protein quantification and statistical analysis were performed with Msstats[105] (version 4.14.0) and LIMMA[106] (version 3.62.1) package in R. Contaminants were filtered, and features were converted to MSStats format for downstream processing. Uninformative features were removed, and missing values were imputed with the 'MBimpute' function within MSStats. Protein abundances were normalized to median and differential expression between groups was evaluated using the empirical Bayes moderated t-tests implemented in LIMMA followed by Benjamini-Hochberg (BH) p-value adjustment. Proteins with adjusted p-value less than 0.05 and a fold change of more than 2 for each comparison were considered as significantly changed. To predict 'strong binders', a cutoff of mean + 3 standard deviation (SD) on the log2 fold change was applied.

PUS10 gene set signature analysis

The PUS10 gene set (PUS10-GS) was obtained analyzing the RNA-seq by DESeq2 with FDR <0.05 and $|\log2FC| > 0.58$ to define ~2500 differently expressed genes. Next, rank-based single sample scoring method, singscore,[103] was applied to determine PUS10 and IFN-alpha[110] gene signature scores for each sample within Systemic lupus erythematosus (SLE),[63] inflammatory bowel disease (IBD)[64] and colon cancer.[65] Only up-regulated genes in *Pus10KO* cells were used as PUS10 gene set to analyze the PUS10-GS score for single-cell datasets of SLE[111] and IBD[112] by Seurat[99] and Scanpy.[100]